Modeling Solar Eclipses at Extreme Ultra Violet Wavelengths and the Effects of Nonuniform Eclipse Shadow on the Ionosphere-Thermosphere system

Sebastijan Mrak[1], Qingyu Zhu[2], Yue Deng[3], Ingolf E. Dammasch[4], Marie Dominique[4], Marc R. Hairston[5], Yukitoshi Nishimura[6], and Joshua Semeter[6]

[1]Space Weather Technology, Research, and Education Center, University of Colorado Boulder, Boulder, CO, USA
[2]National Center for Atmospheric Research, Boulder, CO, USA
[3]University of Texas Arlington, Arlington, TX, USA
[4]Solar-Terrestrial Center of Excellence, SIDC, Royal Observatory of Belgium, Brussels, Belgium
[5]Center for Space Sciences, University of Texas Dallas, Richardson, TX, USA
[6]Department of Electrical and Computer Engineering and Center for Space Physics, Boston University, Boston, MA, USA

Key Points:

- A model of solar eclipses at EUV wavelengths is introduced that takes SDO AIA and GOES-R SUVI images as the input.
- GITM simulations reveal the impacts of the EUV eclipse mask contribute about 20% to the I-T response.
- The EUV eclipse model is validated using PROBA2/LYRA in-situ measurements of solar irradiance flux during eclipse passes.

Corresponding author: Sebastijan Mrak, sebastijan.mrak@colorado.edu

Abstract

The impacts of solar eclipses on the ionosphere-thermosphere system particularly the composition, density, and transport are studied using numerical simulation and subsequent model-data comparison. We introduce a model of a solar eclipse mask (shadow) at Extreme Ultra Violet (EUV) wavelengths that computes the corresponding shadowing as a function of space, time, and wavelength of the input solar image. The current model includes interfaces for Solar Dynamics Observatory (SDO) and Geostationary Operational Environmental Satellites (GOES) EUV telescopes providing solar images at nine different wavelengths. We show the significance of the EUV eclipse shadow spatial variability and that it varies significantly with wavelength owing to the highly variable solar coronal emissions. We demonstrate geometrical differences between the EUV eclipse shadow compared to a geometrically symmetric simplification revealing changes in occultation vary ±20%. The EUV eclipse mask is validated with in-situ solar flux measurements by the PROBA2/LYRA instrument suite showing the model captures the morphology and amplitudes of transient variability while the modeled gradients are slower. The effects of spatially EUV eclipse masks are investigated with Global Ionosphere Thermosphere Model (GITM) for the 21 August 2017 eclipse. The results reveal that the modeled EUV eclipse mask, in comparison with the geometrically symmetric approximation, causes changes in the Total Electron Content (TEC) in order of ±20%, 5-20% in F-region plasma drift, and 20-30% in F-region neutral winds.

Plain Language Summary

Solar eclipses perturb the upper atmosphere by cooling the region under the eclipse shadow due to abated solar irradiance and rarefy the Earth's ionosphere due to reduced photo-ionization under the eclipse's shadow. Solar eclipses are treated as natural laboratory experiments for ionospheric physics because of their predictive nature. Traditionally, the eclipse shadow has been modeled assuming both the Sun and the Moon are circular objects with the Sun being a uniform source of irradiance. This assumption is not correct because the ionosphere is produced by solar X-ray and EUV radiation which primarily originate in the highly variable solar corona. We introduce a model computing eclipse shadow at the EUV wavelength using high-resolution images of the solar corona. The model is validated using EUV irradiance observations from low earth orbit. The impacts of nonuniform EUV eclipse shadow are then investigated with a physics-based global ionosphere-thermosphere model (GITM).

1 Introduction

Solar eclipses have drawn a lot of interest in ionospheric research because they significantly alter the photochemical and transport processes due to the abatement of solar X-ray and Extreme Ultra Violet (EUV) flux within the eclipse's shadow (penumbra). Observations provide exceptional opportunities for testing global models of the ionosphere-thermosphere (I-T) because numerical simulations can be done in advance by virtue of knowing eclipses' timing, duration, location, and magnitude centuries ahead, making eclipses natural experiments. However, the laboratory experiment notion proved very challenging as nicely summarized by Rishbeth (1968): "The ionospheric physicist might wish that the Sun could be regarded as a constant, uniform source of ionizing radiation; but investigations of the Sun show that it is not." The solar corona, the source of the ionizing X-ray and EUV flux is considerably larger than the photosphere, therefore there exist no total solar eclipses for the I-T. Additionally, the solar corona is a spatially nonuniform source of X-ray and EUV radiation with localized regions of intense irradiance (solar active regions) and regions emanating low fluxes (coronal holes).

Even during a maximum eclipse about 10% of the total EUV flux reaches the thermosphere due to intense radiation sources located near the solar limbs (Rishbeth, 1968).

This residual flux was measured by in-situ rockets (Smith et al., 1965), and estimated from E-region density reduction during eclipses using ionosonde measurements of peak E-region electron density (NmE) (Nestorov & Taubenheim, 1962; Taubenheim & Serafimov, 1969; Marriott et al., 1972). Modeling of I-T responses to solar eclipses encompasses the estimation of eclipse penumbra, which is estimated assuming geometrically symmetric celestial bodies with a chosen maximum eclipse occultation factor (EOF) to reflect the residual EUV flux (Deehr & Rees, 1964; E. C. Ridley et al., 1984; Le et al., 2008; Wu et al., 2018; Lin et al., 2018; Bravo et al., 2020). Recently, the maximum EOF was estimated using a realistic EUV model, using images of the solar corona, to obtain an appropriate scaling factor inflating the solar radius using Solar and Heliospheric Observatory (SOHO) Extreme-ultraviolet Imaging Telescope (EIT) (Davis et al., 2000) and Solar Dynamics Observatory (SDO) Atmospheric Imaging Assembly (AIA) (Huba & Drob, 2017; McInerney et al., 2018; Harding et al., 2018).

The non-uniform corona causes transient gradients within the eclipse shadow that were measured in the NmE time-series profiles and attributed to covering and uncovering of solar active regions (Nestorov & Taubenheim, 1962; Rishbeth, 1968; Marriott et al., 1971; Davis et al., 2000). Marriott et al. (1972) utilized NmE-derived EOF from 4 spatially separated ionosondes to reconstruct the positions of solar active regions in solar corona with great success. The covering and uncovering of solar active regions were identified as a salient density perturbation measured by Global Positioning System (GPS) estimated Total Electron Content (TEC) during the 21 August 2017 eclipse (Mrak et al., 2018). The authors showed four large-scale crescent-shaped TEC perturbations that were co-linear with computed spatial gradients in EUV penumbra unambiguously proving the TEC perturbations were due to modulation of the ionospheric production function. Furthermore, measurements on board the Defense Meteorological Spacecraft Program (DMSP) measured transient fluctuations of electron temperature and ion drifts when traversing the regions of steep EUV gradients (Hairston et al., 2018).

We utilize a 4-D (space and time) model of solar eclipse shadow computed from images of the Sun taken by SDO-AIA and GOES-R Solar Ultra Violet Imager (SUVI) telescopes. The model computes EOF as a function of geographic position (latitude, longitude, altitude) and universal time (UT) at a given wavelength specified by the telescope channel. The proof of concept was demonstrated for the 21 August 2017 eclipse using SDO AIA (Huba & Drob, 2017; Mrak et al., 2018; Hairston et al., 2018) in conjunction with Naval Observatory Vector Astrometry Software (NOVAS) (Kaplan et al., 2011). Here we introduce an updated model of eclipse penumbra that works with SDO AIA, Geostationary Operational Environmental Satellites (GOES)-R SUVI, and SOHO EIT images, computing EOFs based on the pyEphem (https://pypi.org/project/ephem/) library with a purely *Pythonic* software framework. The ramifications of using a realistic EUV model of penumbra on the I-T response are modeled with Global Ionosphere Thermosphere Model (GITM). We describe major differences of EUV penumbras compared to the GEO simplification, we validate the computed occultations with in-situ EUV flux measurements and quantify their impacts on the I-T response using GITM.

2 PyEclipse: A computational model of solar eclipses

High-resolution and high-fidelity images of coronal emissions are readily available since the operation of SDO AIA began in May 2010. The SDO AIA provides (4096 x 4096 pixels) images of solar emissions at seven EUV wavelengths (9.4 nm, 13.1 nm, 17.1 nm, 19.3 nm, 21.1 nm, 30.4 nm, and 33.5 nm) at sub-minute resolution per wavelength (Lemen et al., 2012). Another space-based EUV solar telescope is on-board GOES-R series satellites 16 and 17 providing EUV images at 6 EUV wavelengths with the SUVI (9.4 nm, 13.1 nm, 17.1 nm, 19.5 nm, 28.4 nm, and 30.4 nm) with data available since 2016 (GOES-R 16) and 2018 (GOES-R 17) (Darnel et al., 2022). The SUVI images have a resolution of 1280 x 1280 pixels with a 4-minute cadence. GOES-SUVI images have to be taken in

as a level-2 data product to avoid noisy background. Solar EUV images before 2010 are available from the SOHO EIT dating back to 1996. SOHO EIT images have a considerably lower dynamic range compared to AIA or SUVI, so we do not use the images in this report. The model interfaces with EIT, but additional image processing is necessary to obtain science-grade eclipse penumbra. We access level-1 AIA and EIT data through the Virtual Solar Observatory (VSO) using `sunpy` (Barnes et al., 2020), while SUVI data is obtained from National Centers for Environmental Information (NCEI) database. In general, `PyEclipse` can process any image of the Sun in Flexible Image Transport System (FITS) format with metadata providing the position of the center of the Sun (in pixel units), a factor converting pixels to arcseconds in both dimensions, and an angular deviation of the Sun's north pole from the vertical axis.

We developed the `PyEclipse` model based around `pyEphem` library. We compute the positions of the Sun and the Moon using `pyEphem` library that parses astronomical ephemeris with `XEphem` wrapper. The wrapper returns the positions of the Sun and the Moon relative to the observer in Topographic coordinates: the right ascension and declination, and azimuth Φ and elevation ϵ angles. The latter has the same meaning as the former but is defined relative to the observer's horizon. We compute the radial distance between the two bodies using the law of the great circle distance d:

$$d = 2\arcsin\left(\left[\sin^2\left(\frac{\Phi_S - \Phi_M}{2}\right) + \cos(\Phi_S)\cos(\Phi_M)\sin^2\left(\frac{\epsilon_S - \epsilon_M}{2}\right)\right]^{\frac{1}{2}}\right) \tag{1}$$

where subscripts S and M denote the Sun and the Moon, respectively. The bearing angle α between the two objects defined as a clockwise angle from North to East is defined as:

$$\alpha = \arctan\left(\frac{\sin(\Phi_M - \Phi_S)\cos(\Phi_M - \Phi_S)}{\cos\epsilon_M\cos\epsilon_S - \cos\epsilon_M\sin\epsilon_S\cos(\Phi_M - \Phi_S)}\right) \tag{2}$$

For the EUV eclipse occultations using AIA/SUVI/EIT images, we convert the Moon's relative position to the Sun (d, α) into the units of pixels using a constant provided by the EUV image metadata. Lastly, the Sun is rotated for the parallactic angle η based on the observer's local time, and geographic location. The parallactic angle adjusts the position of the apparent Sun's north pole to the direction of the observed zenith located in the northern hemisphere (Meadows, 2007):

$$\cos(\eta) = \frac{\sin(glat) - \sin(\delta)\cos(90 - \epsilon_S)}{\cos(\delta)\sin(90 - \epsilon_S)} \tag{3}$$

where $glat$ is geographic latitude, and δ is solar declination angle. The local time, geographic location, and seasonal dependence on the parallactic angle are described in Appendix Appendix A.

We compute the Eclipse Occultation Factor (EOF) as

$$EOF = \frac{\sum_i N_i}{\sum_i M_i} \tag{4}$$

where i is the pixel number, N is the occulted (masked) image, and M is the unocculted (only the Sun) image. EOF is always less or equal to 1, where the unity denotes no eclipse, and zero is a total eclipse. For the geometrically symmetric eclipse, we compute the EOF as:

$$EOF = 1 - \frac{A}{\pi(\lambda_S r_S)^2} \tag{5}$$

where A is the surface area of the overlapping circles (the Sun and the Moon), with the derivation in Appendix B. The denominator is the area of the Sun, where λ_S is the solar radius inflating factor.

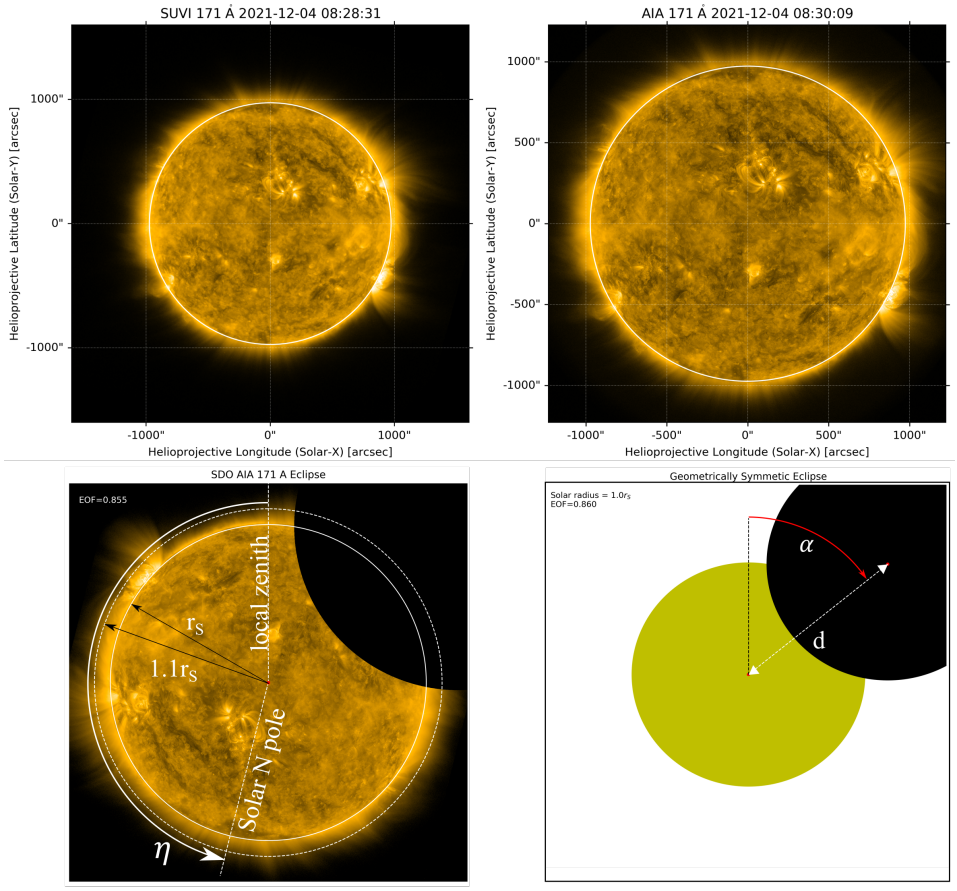

Figure 1. (top) Visualization of the Solar images used to compute high fidelity EUV eclipse using GOES SUVI (left) and SDO AIA (right) during the 4 December 2021 solar eclipse. (bottom) Illustration of eclipse occultation factor (EOF) computation and the depiction of parameters used for the calculations. (left) EOF using SDO AIA 17.1 nm image, rotated for the parallactic angle η. (right) Geometrically symmetric EOF using the distance d, bearing angle α, and the solar radius inflating factor $\lambda_S = 1.1$. The bottom row EOFs were computed from Jang Bogo station in Antarctica (164°E, 74°S).

The chief parameters and the illustration of the input solar images used by the PyEclipse to compute the EOFs are depicted in Figure 1. This figure shows the GOES SUVI and SDO AIA images at 17.1 nm wavelength during the 4 December 2021 polar solar eclipse. Note, that the axes are converted from pixel counts into angular units of arcseconds using the conversion factor provided by the metadata. The white fiducial line depicts the classical solar radius $r_S = 695{,}700$ kilometers, which is the radius of the photosphere. The bottom panels depict a computation of the EOF using a EUV image (left) and the geometrically symmetric configuration (GEO) of the Sun and the Moon (right). The SDO AIA image is first rotated for the parallactic angle η, then the image is masked by the Moon. This panel indicates the classical solar radius (thick white line) and an approximation of the ∼10% wider EUV radius (depending on the solar activity), which corresponds to the 1,000,000 degrees Kelvin solar corona. Note that the parallactic angle is close to 180 degrees because this was computed at a location in Antarctica (Jang Bogo station), where the observer's zenith is closely aligned to the Sun's south pole. The bot-

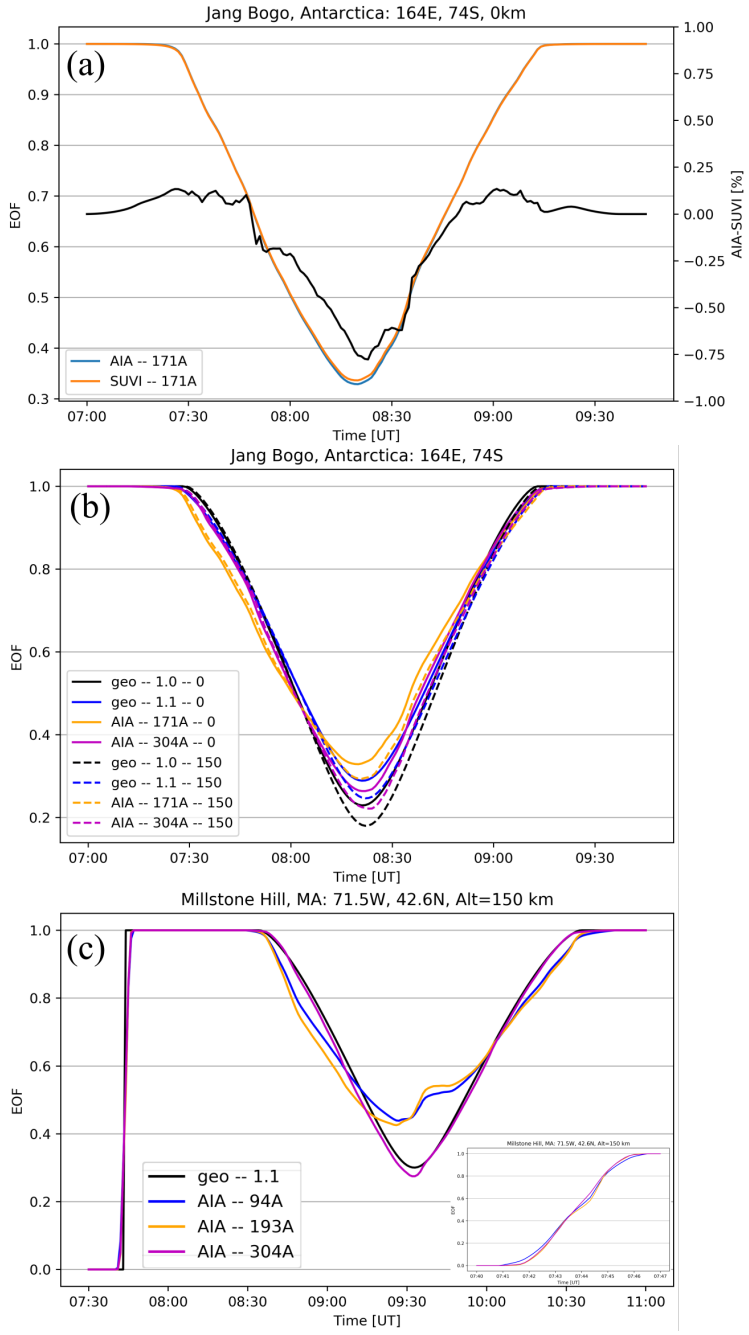

Figure 2. Eclipse Occultation Factors (EOFs) computed using PyEclipse for two eclipses and for a fixed geographic location. (a) EOFs during the 4 December 2021 eclipse are based on SDO AIA (blue) and GOES SUVI (orange) EUV images at 17.1 nm. The black line is the relative difference between the two EOFs. (b) EOFs during the 4 December 2021 eclipse corresponding to different wavelengths and solar radii at two altitudes (solid vs. broken lines). (c) EOFs for the 10 June 2021 eclipse near sunrise, illustrating the horizon effect (zoomed in the bottom right part of the figure) and the wavelength dependence.

tom right panel depicts the positions of the eclipsed bodies and the parameters α, and d used to compute the EOF.

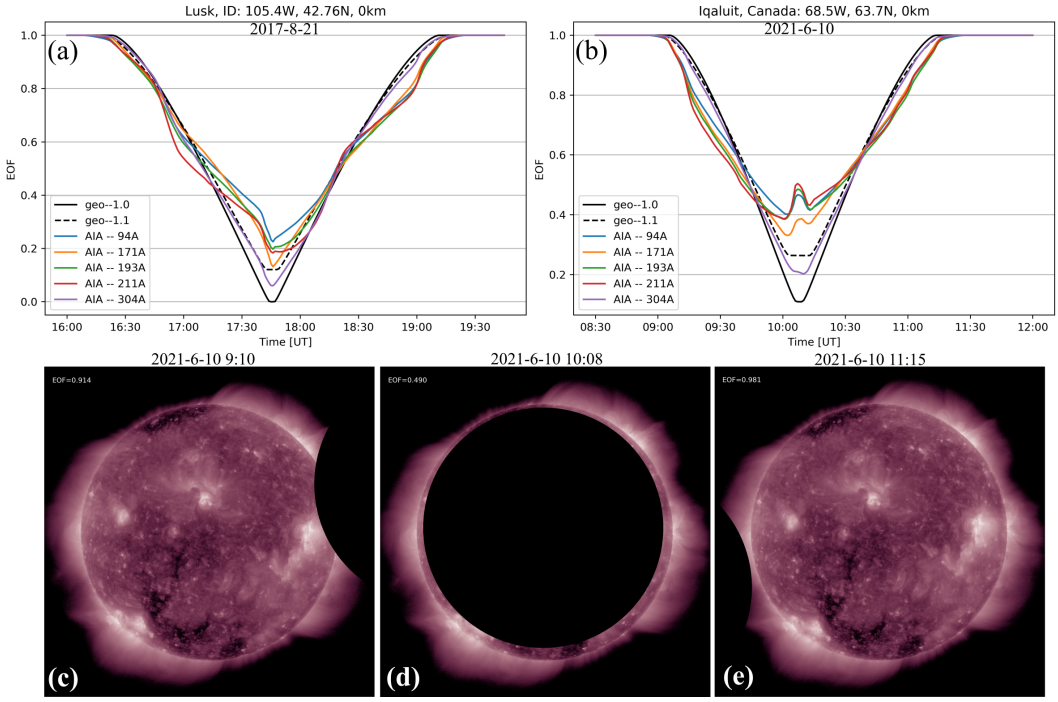

Figure 3. (a–b) Wavelength dependence and the consequences of solar active regions on the EOF. (a) EOFs from SDO AIA EUV telescopes and uniform geometrical eclipses (GEO) at two solar radii during the 21 August 2017 eclipse in Lusk, Idaho. (b) The same as in (a) but for the 10 June 2021 eclipse from Iqaluit, Canada. (c–e) Computed images of the solar eclipse using 21.1 nm SDO AIA telescope at three epochs from the location with depicted EOFs in panel (b).

Examples of EOFs computed by the PyEclipse model are depicted in Figure 2. The top panel (a) depicts the computed EOF at 17.1 nm wavelength for the Jang Bogo Antarctic station for the 4 December 2021 polar eclipse. The orange and blue time-series traces were computed using GOES-SUVI and SDO-AIA images, respectively. The black line represents the relative difference between both time-series. The difference never exceeds 1%. The middle panel (b) depicts the wavelength and altitude dependence at the same geographic (longitude/latitude) location. Solid lines are EOFs computed for different wavelengths and a uniform solar radius at the ground level, and the broken lines depict the corresponding EOFs at 150 km altitude. This particular example shows that, at this location, the maximum EOF was smaller at 150 km (greater eclipse), but this does not imply the general pattern. The height dependence is well known due to the solar zenith angle dependence (T. G. W. Verhulst & Stankov, 2020), and it depends on the relative position of the observer. This panel furthermore illustrates the wavelength dependence of the EOF, which was evident even during a solar minimum. The difference in solar radii between different EUV wavelengths is normally of the order of 10%. Lastly, the PyEclipse is computing the position of the horizon, which is superposed on the normal eclipse mask if the horizon and the solar eclipse are simultaneously in the field of view. Figure 2c shows the continuous horizon (sunrise) just prior to an arriving eclipse and its wavelength dependence, as observed from the Millstone Hill Observatory during the 10 June 2021 eclipse.

3 Spatiotemporal variability of the EUV penumbra

Figure 2c image depicts anomalous wavelength-dependent EOF variability near the anticipated maximum eclipse (minimum EOF). The sudden changes in the EOF, which are also visible in Figure 4, are due to covering and uncovering solar active regions. The example from 21 August 2017, was discussed by Mrak et al. (2018) in detail. They have shown that the transient fluctuations of the EOF resulting from covering and uncovering the active region cause large-scale effects that are clearly visible in the GPS-TEC maps. The actual EOF values are highly wavelength dependent as depicted in Figure 3a, with variations exceeding 15% at the most dramatic point just before the maximum eclipse owing to a solar active region at the limb of the Sun (Mrak et al., 2018). Figure 3b shows a wavelength-dependent sudden increase in the order of 5-10%, at a place one expects the maximum eclipse. This is explained in the reconstructed eclipse images in Figure 3c–e. This eclipse took place during the time that the solar EUV emissions predominantly originated in the regions near the solar limb. The sequence of three images shows that during the first half of the eclipse, the main source of the EUV (originated near the western limb) was constantly occulted (panel c). During the time that the Moon covered the biggest area of the Sun (panel d), both limbs were uncovered causing an actual increase in the solar EUV flux. During the second part of the eclipse, when the Moon was transitioning away, the Moon occulted the eastern limb causing the initial decrease in the EOF before it uncovered a sufficient area of the Sun for the EOF to recover.

Time-series line plots in Figure 2b-c and Figure 3a-b furthermore depict the differences between the EOFs computed using the simple geometric (GEO) consideration and the actual eclipse at EUV wavelengths. We already demonstrated that the solar corona extends approximately 10% beyond the standard solar radius. Therefore, the difference in the minimum EOFs (i.e., maximum eclipse) between the EUV EOF and a GEO EOF computed using the standard solar radius (denoted as GEO 1.0) is expected. While the increase in the effective solar radius causes a larger minimum EOF, it might also distort the EOF profile in the vicinity of the maximum eclipse as depicted in Figures 3a-b in black-dashed lines. The radius inflation causes the EOF to flatten over a period of several minutes. This causes an artificially high impact on the ionospheric density reduction as explained in section 5.4. The paradigm of assuming solar eclipses as spherically symmetric and occultation masks with a pre-defined minimum occultation in the order of 10% was established in the 1960s (Rishbeth, 1968). This consideration has persisted until the present day, as eclipse occultation models are still commonly computed assuming geometrically symmetrical celestial bodies.

Another pin-hole projection example occurs when a relatively strong solar active region (compared to the surrounding area) is located on a limb. That solar active region creates a transient perturbation near local noon, at the edge of the penumbra where the Moon skims only over the edges of the solar corona. This effect is presented in Figure 4 time-series accompanied by a sequence of reconstructed images of the eclipse using the SDO AIA telescope. The time series in Figure 4a shows a sudden, wavelength-dependent, drop in the EOF at around 18:45 UT, which lasted just 5 minutes. The total drop was the biggest at 19.3 nm wavelength, reaching $\sim$12% below the baseline set by the 10% inflated GEO mask. The reconstructed eclipse images in panels b–e show the source of this depletion was a sudden occultation of one solar active region located on the limb. The Sun is rotated by the parallactic angle.

The importance of accurate EUV eclipse modeling at large scales is presented in 2D maps. Figure 5 shows geographic projections of two solar eclipse masks, 21 August 2017 in the top and 10 June 2021 in the bottom row, at one epoch computed using 10% inflated geometrically symmetric approximation (GEO 1.1 - left column), and 9.4 nm SDO AIA (middle column). The right column is the difference between the GEO and EUV masks. The difference maps show that (1) GEO approximation overestimates and underestimates by $\pm$15-25% the EUV eclipse occultation depending on the position within

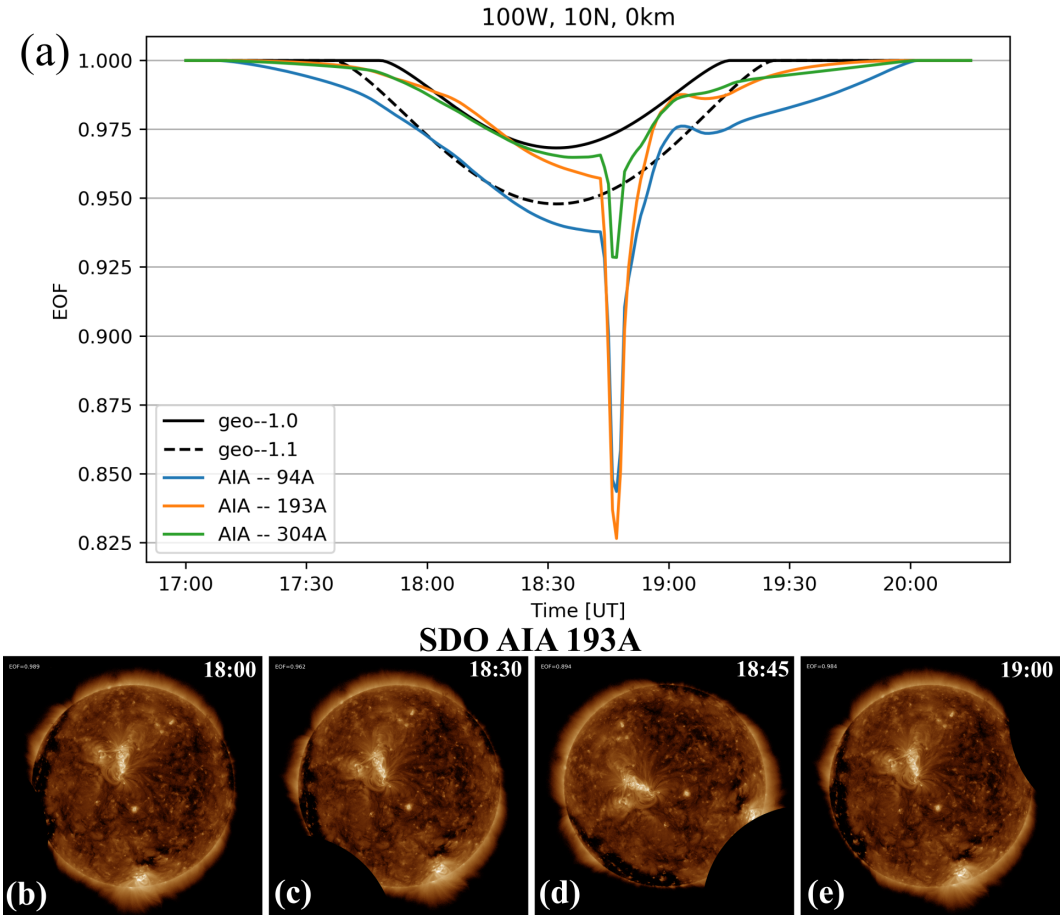

Figure 4. (Eclipse Occultation function (EOF) during the 21 August 2017 eclipse at 100°W, 10°N. (a) Shows EOF time-series at different wavelengths and 2 different solar radii factors. The EUV EOFs from SDO AIA images depict a transient reduction of EOF near 18:45 UT. (b–e) The sequence of reconstructed eclipse images shows the transition of the Moon skimming over one solar active region located on the solar limb.

the penumbra, (2) EUV masks feature regional transient feature discussed with Figure 4, and (3) the positions of the maximum eclipse (i.e., minimum EOF) differ and the difference changes with time.

The solar eclipse mask varies in altitude as described in detail by T. G. W. Verhulst and Stankov (2020). We bolster their findings by expending the height dependence analysis using solar EUV emissions. Figure 6 shows the same eclipses and the exemplary eclipse masks as in Figure 5 in the latitude-altitude projection. The figure shows significant position-dependent differences between the uniform and the EUV masks in the last column. The differences in the order of ±15% alternate as a function of latitude every 5-10 degrees (i.e., 500 - 1,000 km). The 10 June 2021 eclipse EUV panel in Figure 6e shows the altitude-dependent projection of solar active regions near 60°N which was identified in Figures 3, and 5e-f. The altitude dependence, especially for eclipses similar to the 10 June 2021 eclipse mask emphasizes the importance of using a 3-D eclipse mask in global modeling. However, the latter task is not trivial because the eclipse masks are specified at the upper boundary conditions together with the incoming EUV irradiance flux in a global circulation model. This also raises the question of what is the most appropriate

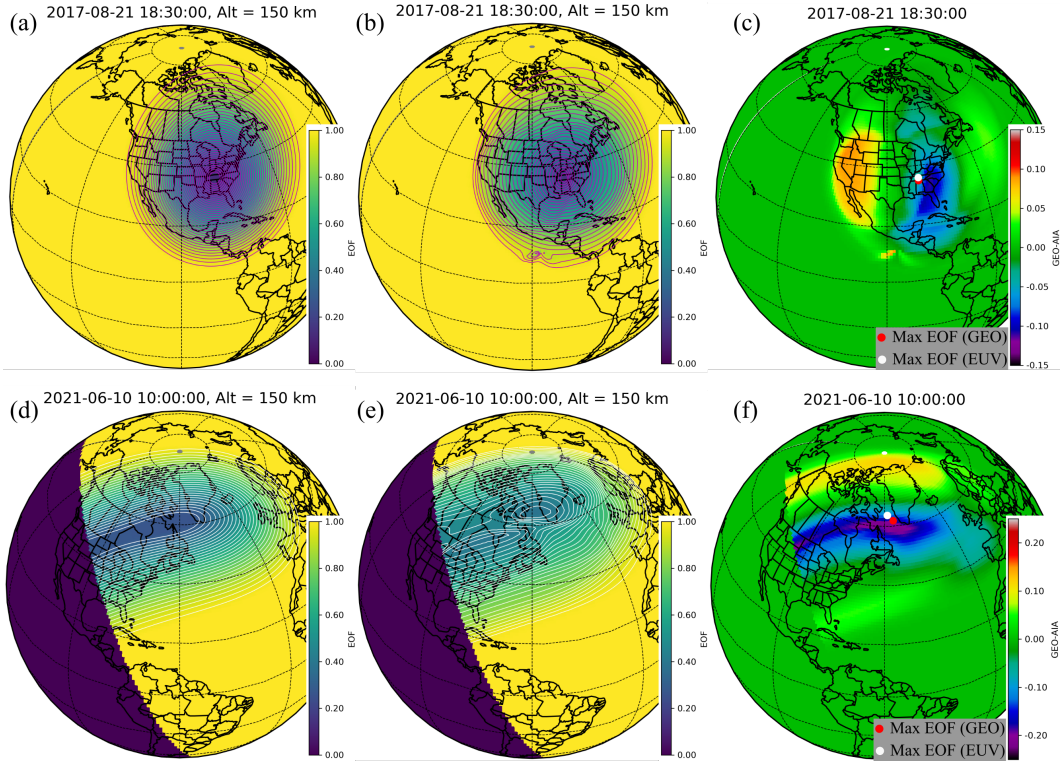

Figure 5. 2-dimensional latitude-longitude eclipse masks for two eclipses (top/bottom columns). (a–c) 21 August 2017 eclipse masks at 18:30 UT: (a) uniform mask with 10% inflated solar radii (GEO 1.1), (b) EUV mask using 9.4 nm SDO AIA image, (c) difference between (a) and (b). (d–f) 10 June 2021 eclipse masks at 10:00 UT: Rows are in the same format as the top panel. Different contour colors are for improving contrast and highlight the different features. Red/White dots in panels c and f the last row denote the maximum eclipse (minimum EOF) of the GEO and EUV masks, respectively.

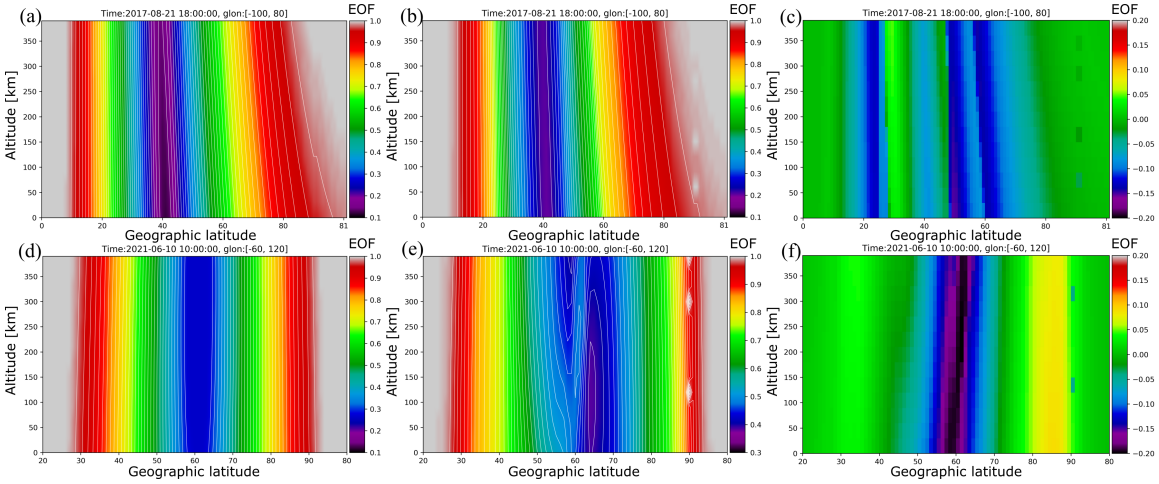

Figure 6. 2-dimensional latitude-altitude eclipse masks in the same format as for the eclipse from in Figure 5).

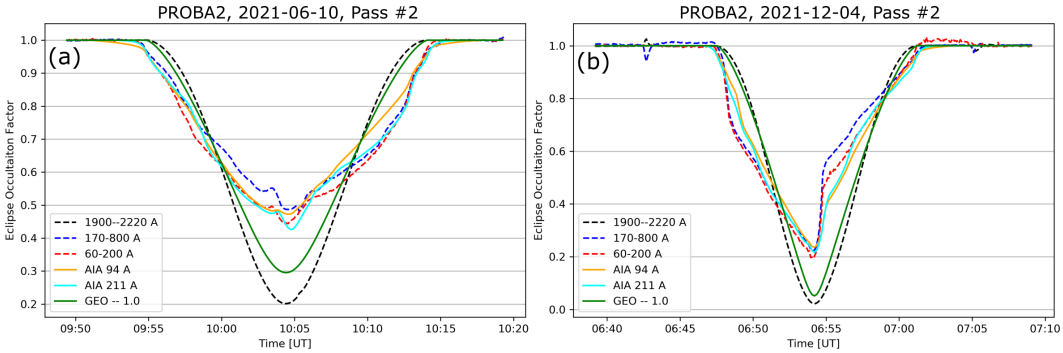

Figure 7. PROBA2/LYRA observations of the relative decrease in irradiance flux (dashed lines) compared to the PyEclipse model (solid lines) during one pass through the 10 June 2021 (a), and 4 December 2021 (b) eclipse. Colors represent three different LYRA wavelength bands (channels): (blue) LYRA 6-20 nm, (red) LYRA 17-80, and (black) LYRA 190-220 nm. Modeled EOFs were computed using PyEclipse wavelengths: (orange) SDO AIA 9.4 nm, (cyan) SDO AIA 21.1 nm, (black) GEO 1.0.

altitude for computing the 2D (lon/lat) eclipse mask knowing the systemic altitude-dependent trend (T. G. W. Verhulst & Stankov, 2020): at the E-region height where the impacts in plasma production and loss are the most significant, or at the height of the model's upper boundary condition?

4 Validation

We validate the PyEclipse EUV masks with direct measurements of solar irradiance using the PRoject for Onboard Autonomy 2 (PROBA2) Large Yield Radiometer (LYRA) (Dominique et al., 2013; BenMoussa et al., 2009). LYRA includes 4 photometers out of which we use 3: (1) 190-222 nm Herzberg continuum channel, (2) 17 - 80 nm + X-ray below 5 nm channel, and (3) 6 - 20 nm + X-ray below 2 nm. For this study, we used the data from the backup unit of LYRA (unit1), which is the least degraded. LYRA data were calibrated by subtracting dark currents for each channel. Then the data were decimated from the original 20 Hz to 2 Hz, and the irradiance flux was normalized by setting it to 1.0 adjacent to the eclipse transition. This procedure was applied in previous studies (Stankov et al., 2017).

PROBA2 passed the 10 June 2021 and the 4 December 2021 eclipses three times with the second pass being the longest and at the highest solar zenith angle. We compare LYRA measurements taken from the second passes of each eclipse and converted them into eclipse occultation factors as described earlier. These observations are compared with the PyEclipse-modeled EOF at three wavelengths along the satellite trajectory. This comparison is presented in Figure 7. We use LYRA observations from the Herzberg continuum channel 1, X-ray+EUV channel 2, and X-ray+EUV channel 3. The modeled EOFs are computed using a geometrically symmetric mask with non-inflated solar radius (GEO 1.0), SDO AIA 9.4 nm, and SDO AIA 21.1 nm channels. All comparisons show the same trend and very similar maximum occultation. The difference in the maximum occultation can be accounted for by virtue of using an arbitrary detrending of LYRA measurements, and a slightly different effective radius for the Herzberg continuum whose source region apparently dims toward the limb of the Sun causing a bigger maximum eclipse compared to the GEO 1.0 calculation. The only considerable difference is in the covering/uncovering of the solar active regions. While the model reproduces the timing and duration of the eclipse mask transients, the repose time is slower for both cases. This

can be explained by a couple of different factors: (1) The AIA images have finite spatial resolution and dynamic range smearing out sharp brightness transitions. (2) PyEclipse model is purely geometric, it does not consider any diffraction of the Moon limb. (3) LYRA detectors are aging, even those on the backup unit, and are losing sensitivity over time that might reflect sharper changes (BenMoussa et al., 2013). (4) The LYRA wavelength response is different from the SDO AIA narrowband telescopes, and LYRA is sensitive to soft X-ray bands while SDO AIA does not cover these wavelengths. In aggregate, the in-situ observations of abated solar irradiance are morphologically replicated by the PyEclipse model, the timing and duration of overall eclipse shadow as well as the transient perturbations are in agreement. If the model misses anything, then these are only very steep transitions which would lead to a slight underestimation of the modeled gradients using PyEclipse eclipse masks.

5 Modeling I-T response to the 21 August 2017 eclipse

The impact of a EUV (9.4 nm) eclipse mask compared to the uniform (GEO) eclipse mask on the I-T system was investigated using the Global Ionosphere Thermosphere Model (GITM) (A. Ridley et al., 2006). GITM is a 3D non-hydrostatic GCM that self-consistently solves the neutral and ion densities, composition, velocities, and temperatures on an adjustable spatial and temporal resolution. GITM differs from other GCMs in that it can simulate the non-hydrostatic processes caused by the variation of energy inputs (Deng et al., 2008, 2011, 2021; Lin et al., 2017, 2018; Zhu et al., 2017). The electrodynamic solver in GITM used in this study is the NCAR 3D dynamo solver (Maute & Richmond, 2017) which was coupled by Zhu et al. (2019).

Three simulations are carried out: one is the controlled run where no eclipse mask is included; another two simulations are eclipse runs where the GEO and EUV eclipse masks are included. The way to introduce the time-evolving eclipse mask is similar to that in Lin et al. (2018) where the eclipse mask is spatiotemporally interpolated to the GITM grids and model running time during the simulation. Hence, an EOF can be obtained at a grid and a model running time which is then multiplied by the EUV flux, derived from the F10.7 on that day, to calculate the ionization and heating due to the EUV radiation using Torr et al. (1979). For all GITM runs, the spatial resolution is 2.5° in longitude, 1.25° in latitude, and 1/3 scale height in altitude, the temporal resolution is 2s and the output cadence is 10 min. The high-latitude electric field and electron precipitation are specified by the Auroral Spectrum and High Latitude Electric field variability (ASHLEY, Zhu et al. (2021)) model, which is driven by the realistic interplanetary magnetic field (IMF) and solar wind data. GITM has been used before to study the global response to the 2017 eclipse (Cnossen et al., 2019), model-data comparison (Wu et al., 2018), and to identify small-scale wave-like features (Lin et al., 2018). The exact comparison between the previous runs is not possible due to the simplified eclipse trajectory (Wu et al., 2018). We show only modeling results of the 21 August 2017 eclipse and compare them to observations in the literature to quantify the contribution of the EUV mask to the I-T response compared to the uniform eclipse assumption. Other eclipses discussed in the previous sections deserve separate model-data investigations because of the unique features associated with each eclipse.

5.1 Total Electron Content

We present the modeled GITM TEC response in Figure 8. In all GITM figures, the left column represents the difference between the GITM eclipse run using a 9.4 nm EUV mask and the baseline run without the eclipse (eclipse_euv - baseline). The right column is the contribution of the EUV variability demonstrated by the difference plots obtained by GITM eclipse runs using the EUV mask and a geometrically symmetric (GEO) approximation with 10% inflated solar radius (eclipse_euv - eclipse_geo). First, the GITM

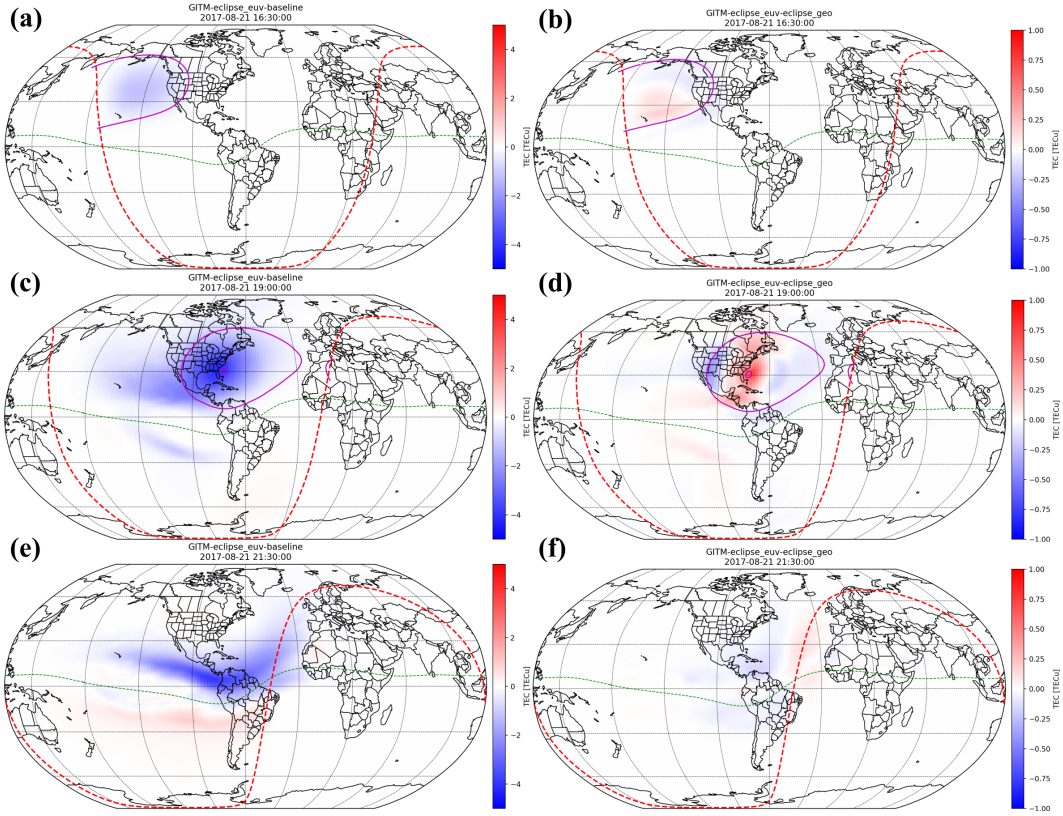

Figure 8. GITM modeled TEC during the 21 August 2017 eclipse. (a, c, e) TEC changes were caused by an eclipse with a 9.4nm EUV mask compared to a baseline run without the eclipse. (b, d, f) TEC changes caused by the EUV mask compared to the uniform eclipse mask assuming symmetric Sun with inflated solar radius by 10%. The red dashed line is a solar terminator at 100 km altitude. The Green dashed line is the magnetic equator. The purple contour denotes the EUV eclipse at EOF=0.9.

results show the increasing depletion growing within the eclipse's shadow reaching ∼5 TECu. The TEC depletion was then trailing the eclipse pass at low latitudes, where the northern ionospheric crest density remained depleted even after the eclipse was gone (bottom panel). This is consistent with reported observations (magnitude 5-7 TECu) and the zonally-elongated depletion at lower latitudes (Coster et al., 2017; Cherniak & Zakharenkova, 2018). Interestingly, the southern crest was first slightly negative (panel c) followed by a positive bay afterward. TEC observations from the southern hemisphere reported TEC depletion at low-latitudes (Zhang et al., 2021) and both depletion and increase at higher latitudes (He et al., 2018). These results reinforce the TEC data assimilation results indicating early reduction followed by the relative increase in the southern equatorial ionization anomaly (EIA) crest (Chen et al., 2019). The right column depicts the difference between using a simple uniform mask and an eclipse mask at EUV wavelengths. The salient finding is that the use of the EUV mask contributes to as much as ±1 TECu difference at a one-time instance (panel d) which corresponds to ±20% of the total TEC depletion. The biggest difference occurs when an eclipse is near local noon (e.g., panel d). Moreover, Figure 8d shows the difference-TEC gradients resemble the projection of solar active regions (Mrak et al., 2018; Hairston et al., 2018). Animation showing TEC perturbations for the whole eclipse pass is available as a supplemental movie S1.

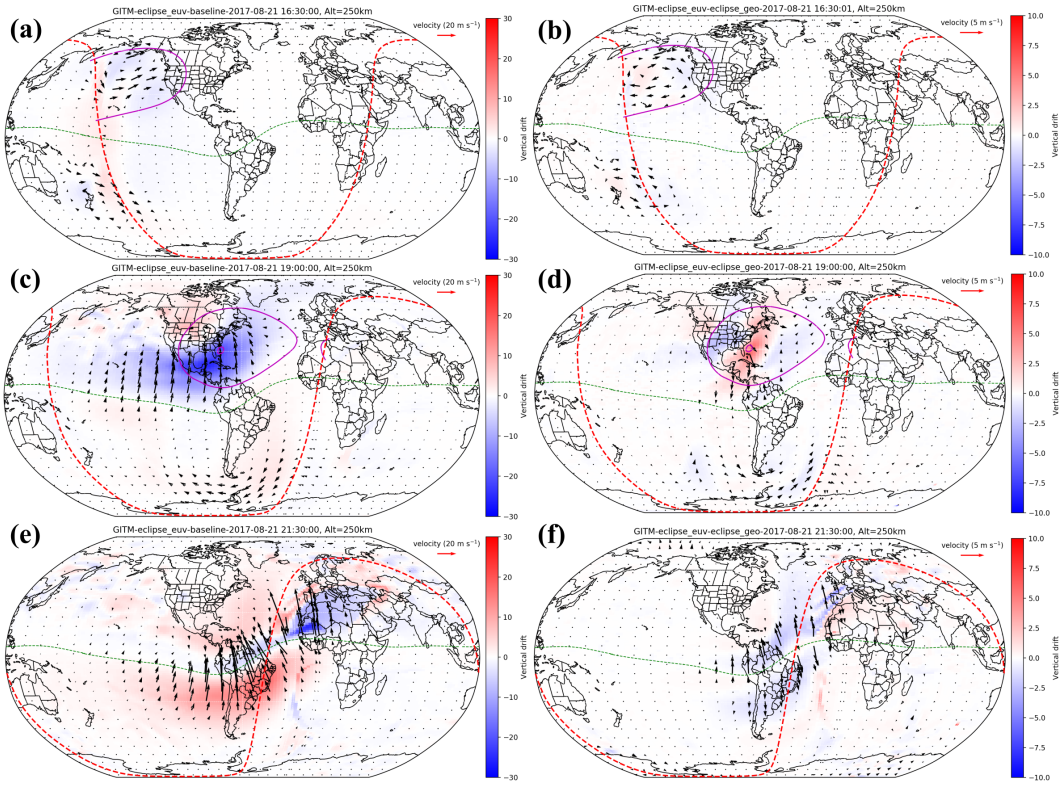

Figure 9. GITM modeled plasma drift at 250 km during the 21 August 2017 eclipse. The format is the same as in Figure 8, horizontal wind scale is at the top right of a panel. Color represents vertical plasma drift.

5.2 Plasma drift

The F-region plasma drift at 250 km altitude is depicted in Figure 9. The model results indicate the eclipse caused global plasma redistribution lasting even after the eclipse was gone. First, panel (a) at 16:30 UT shows the eclipse interacted with the sunrise terminator (red-dashed line) and that it had a weak conjugate effect. During the daytime eclipse transition, the horizontal drift was converging towards the maximum eclipse occultation, with downward plasma drift exceeding 10 m/s (negative velocity). The plasma drift maximized when the eclipse interacted with the sunset terminator and the equatorial electrojet shown in panel (e). The horizontal drift maximized in the vicinity of the magnetic equator, several degrees longitude into the night side with predominantly northward horizontal drifts of the order of 50 m/s and vertical drifts exceeding 20 m/s downward at the equator and upward at both EIA crests. Although the solar eclipse occurred in the northern hemisphere, the impacts are also present in the southern hemisphere because the hemispheres are electromagnetically coupled through closed field lines. Additionally, the dynamo electric field changed due to eclipse-induced neutral wind changes leading to changes at low-latitudes on both sides of the equator. The neutral wind can impact the plasma drift in two ways: 1) change the neutral dynamo electric field; 2) neutral-ion drag force directly impact plasma drift. The contribution of the EUV mask on the plasma drift was in the order of 5%-20% with the maximum contribution to the vertical drift during the daytime (panel d) and to the horizontal drift when interacting with the sunset terminator and the equatorial electrojet. The animation is available as a supplemental movie S2. The morphology of the plasma drift did not change significantly with altitudes above 250 km, except that the drift's magnitude increased with height.

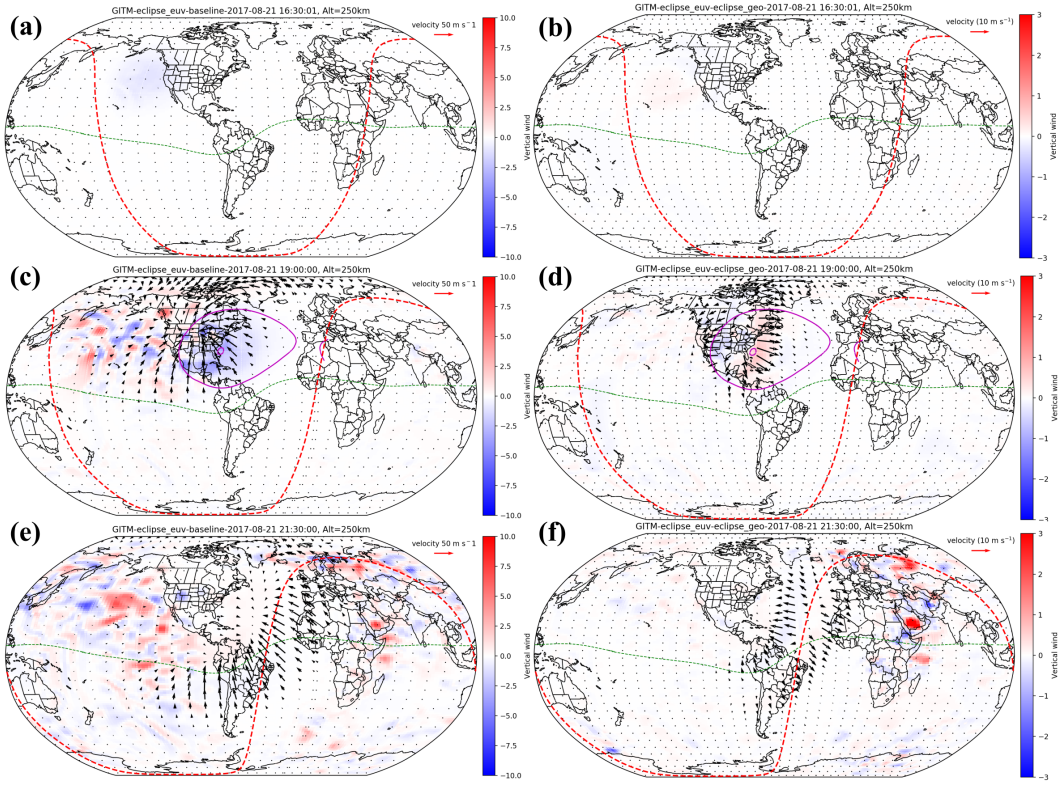

Figure 10. GITM modeled neutral wind at 250 km during the 21 August 2017 eclipse. The format is the same as in Figure 9, horizontal wind scale is at the top right of a panel. Color represents vertical winds.

5.3 Neutral winds

The neutral response to the eclipse is depicted in Figure 10. It can be observed that the eclipse caused a global thermospheric response to the cooling within the eclipse penumbra as shown by other authors (Wu et al., 2018; Cnossen et al., 2019; Harding et al., 2018). This cooling caused the neutral winds to converge toward the maximum eclipse with the biggest perturbation winds located in the leading half of the penumbra. The neutral response extended to the polar region and beyond the northern hemisphere as depicted in panel (c) making the eclipse response global. When the eclipse started to fade away, a large-scale bow-shaped wave-like traveling atmospheric disturbance emerged (panel e) that propagated into the nighttime and to the southern hemisphere as previously shown with observations (Harding et al., 2018) and numerical models (Dang et al., 2018; Lin et al., 2018). Significant activity in the vertical winds was present both on the eclipse trajectory, mainly lagging the penumbra, and on the nighttime hemisphere. While the former was previously explained with GITM simulations (Lin et al., 2018), the latter hasn't been reported. In comparison, a hydrostatic model showed just a smooth trendline (Dang et al., 2018). These waves were present in the night-time hemisphere and lasted for hours after the eclipse was gone. This indicates that some of the observations from Europe (T. G. Verhulst & Stankov, 2018) and from nighttime post-eclipse (Aryal et al., 2019) could be directly associated with the global thermospheric wind response. This feature is likely related to the global neutral wind response over the northern pole. The contribution of the EUV eclipse mask was more prominent compared to the plasma drift: the amplitude of horizontal wind was reduced by 20-30% (the vectors point in the opposite direction

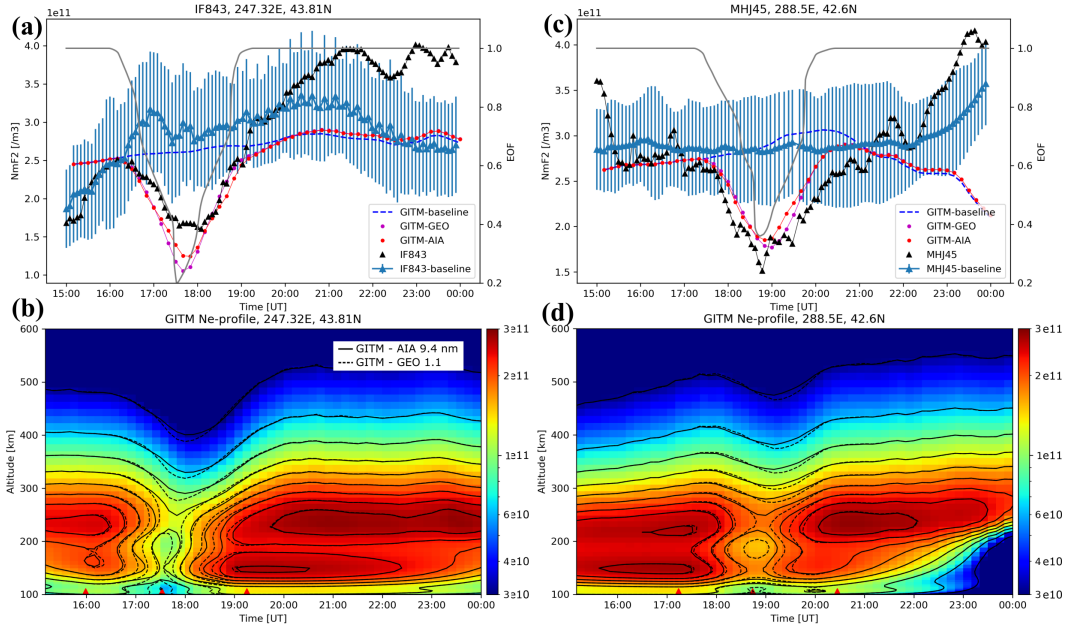

Figure 11. Ionosonde observations of NmF2 from Lusk, Idaho (left, IF843) and Millstone Hill (right, MHJ45) compared to GITM simulation outputs. The top row consists of time-series profiles of observed NmF2 (black), modeled GITM-AIA NmF2 (red), and modeled GITM-GEO NmF2. The blue-dashed line is GITM NmF2 without any eclipse mask. Light blue points are average NmF2 observed by the ionosonde in August 2017 with the corresponding spread represented by ±1 standard deviation. The gray line is the 9.4 nm eclipse occultation function. The bottom tiles are vertical density profiles from GITM simulations. The heat maps are from the GITM-AIA run. Contours represent altitudes of constant density, solid lines from the GITM-AIA run, and the dashed line from the GITM-GEO run.

to the background trend) compared to the use of the GEO mask. The animation showing full thermospheric wind perturbations is available as a supplemental movie S3.

5.4 Height-dependent electron density

The height-dependent density response to the solar eclipse and comparison with ionosonde observations at Lusk, Idaho, and Millstone Hill, Massachusetts is depicted in Figure 11. The top panels show a trend of the peak F2-region density (NmF2) and standard deviation for the month of August 2017 (minus the eclipse day) in blue and the eclipse-day observation in black. The NmF2 inferred from GITM runs using EUV 9.4 nm and GEO 1.1 masks and no eclipse (baseline) are plotted for comparison. In the bottom panels, we plot the electron density profile from GITM simulations. The NmF2 observations and GITM simulations indicate the lag between the maximum eclipse and the peak NmF2 depletion to be in the order of 15-30 minutes. The general trend in the observed NmF2 has been elaborated before (Wu et al., 2018; Reinisch et al., 2018) so we focus on the differences caused by the two eclipse masks. The differences are due to the plateau in the GEO EOF due to the increased solar radius as discussed in Figure 3. This caused bigger maximum depletion at both locations compared to the SDO AIA mask. The smaller depletion caused by the SDO AIA mask was closer to observations. There are some distinct differences between the model results and observations with the most profound difference being the post-eclipse increase in density and signatures of waves – specifically

at Millstone Hill. These features are described and elaborated in the literature and are beyond the scope of this paper focusing on the eclipse mask and the associated local response to abated EUV.

Vertical density profiles at both locations are depicted in the bottom row of Figure 11. Contours mark the altitudes of constant density over time, where the solid lines are from the GITM run with the EUV mask and the dashed lines are from the GITM-GEO 1.1 run. Both locations show that the GITM-GEO caused bigger density depletion at all altitudes. The biggest differences are observed at altitudes below 200 km due to a rapid response of molecular ions to a different shape of incoming irradiance. The magnitude of density reductions varies with altitude and time because the recombination time-constant is increasing with height yielding a slower response to the abated EUV flux. During the recovery, the F1 density in Idaho was higher compared to the F2- region density following the maximum eclipse (second red ticker on the x-axis), whereas this was not the case at Millstone Hill (panel d). The result from Lusk, Idaho, is in agreement with the observed G-condition, that is a situation where NmF1≥NmF2, from Wyoming ionosonde measurements (Bullett & Mabie, 2018) and historical literature (Rishbeth, 1968).

6 Summary

We introduced a computational model of solar eclipse masks PyEclipse, that computed eclipse occultation factors as a function of geolocation, time, and wavelength. The eclipse occultations can be computed using the traditional approach assuming a geometrically symmetric Sun with a variable radius. In addition, PyEclipse computes EUV eclipses at 9 wavelengths using SDO AIA and GOES-R SUVI telescopes. We discuss spatiotemporal features of EUV masks, featuring overall slightly different eclipse occultation gradients compared to the GEO mask, and spatiotemporal gradients due to projections of solar active regions. The differences between EUV and GEO masks depend on solar activity and depends on EUV wavelength. We show that in general the uniform GEO mask overestimates and underestimated the EOF by ±20%, that the position of the maximum eclipse and varies wand is wavelength dependent and that the eclipse mask varies with altitude owing to the solar active region projection. The spatiotemporal morphology of modeled eclipse mask was validated using in-situ observations from PROBA2 spacecraft. We identified that the modeled EOF follows the observations. The model captures the eclipse magnitude as a function of wavelength, timing, and duration of transients. The instantaneous response to these transients, however, lags the magnitude of observed changes.

The effects of EUV spatiotemporal variability were assessed with GITM using the 21 August 2017 case study. We identified that the EUV mask contributed up to ±20% in TEC changes, 5-20% in the F-region plasma drift changes, and 20-30% in the neutral wind response. These results bolster the need for using EUV masks for eclipse simulations and data-model comparison. We compared the plasma response with two ionosondes. The modeled NmF2 decrease with the EUV mask was smaller in magnitude but had a slower recovery compared to the GEO mask. While these modeled changes might be perceived as small, the impacts of the transient gradients in the ionospheric density create spatial gradients in ionospheric conductance which controls how magnetospheric current close, thereby directly affecting the magnetosphere-ionosphere coupling during eclipses occurring at high-latitudes.

7 Open Research

PyEclipse is open source software, available from GitHub https://github.com/aldebaran1/PyEclipse (Mrak, 2022). All eclipse masks used in this paper can be reproduced using the PyEclipse software package. GITM simulation outputs used in this study are available from NCAR GDEX https://doi.org/10.5065/1mtb-e447. Calibrated PROBA2/LYRA data and ionosonde data files are available from Zenodo: https://doi.org/10.5281/zenodo.7042037

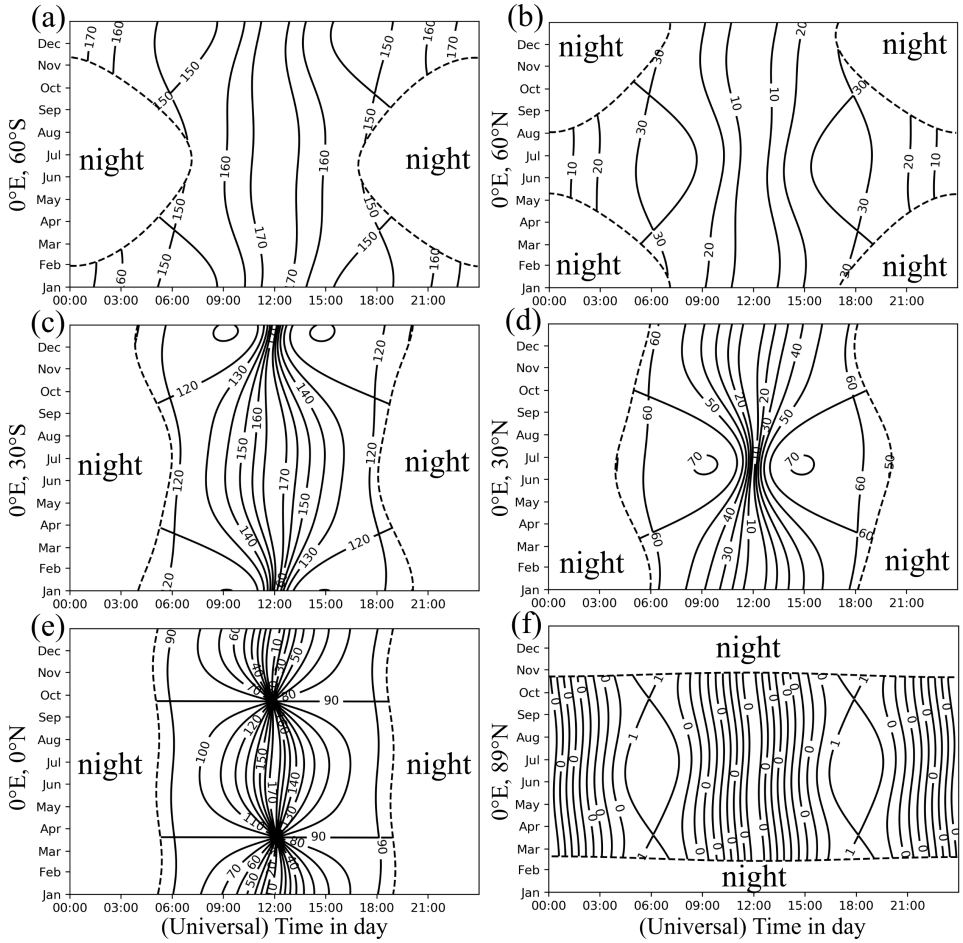

Figure A1. Parallactic angle as a function of time in a day (x-axis), time in a year (y-axis), and different geographic latitudes (a –f) at the zero longitudes (the Greenwich meridian). Dashed lines denote the line of solar zenith angle at 90 degrees (solar terminator).

Appendix A Parallactic angle

The impact of parallactic angle η on the observer in the Earth's inertial coordinate system was introduced by Meadows (2007). We depict its local time, seasonal and latitudinal dependence in Figure A1. The magnitude of the parallactic angle and its rate of change highly depends on the latitude. The biggest rate of change occurs just around 12 noon when the location of the observer crosses the sub-solar point. At the equator, the magnitude of η changes considerably with the season: There is no change in η during equinoxes, while η changes by $\pm 90°$ during solstices. The magnitude, rate of change, and seasonal dependence reduce closer to the poles. At the poles, η is constant throughout the year and day, during polar summer. This is because an observer sitting at the pole has the local zenith always aligned with the Sun's pole. Either looking in exactly the same direction when at the north pole ($\eta = 0$) or exactly in the opposite direction at the sought pole ($\eta = 180$).

Appendix B EOF of a geometrically symmetric eclipse

The geometrically symmetric eclipse is a spherical geometry exercise where the eclipse occultation is a ratio of the occulted area A (area of two overlapping circles) over the

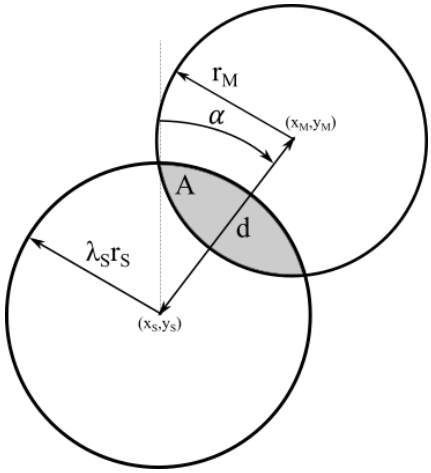

Figure B1. Illustration of the geometrically symmetric eclipse calculation with the Sun (subscript S) and the Moon (subscript M) assumed as circles. The distance d, and the bearing angle α are computed using the spherical geometry formulae. The resulting eclipse occultation function is the area of the circles' overlapping region, i.e., the shared area.

area of the Sun derived in Section 2, Equation 5. The illustration of this problem is depicted in Figure B1. Here, the bearing angle α between the Sun and the Moon was defined in Equation 2 and the distance d between the centers of the bodies in Equation 1. In the calculation of the overlapping area A we assume the position of the center of the Sun $(x_s, y_s) = (0, 0)$. The position of the center of the Moon (x_m, y_m) is computed via the coordinate transformation from d, α:

$$x_m = \arctan\left(\frac{\sin d \sin\alpha}{\cos d}\right) \tag{B1}$$

$$y_m = \arcsin\left(\sin d \cos\alpha\right) \tag{B2}$$

Then, the overlapping area A is

$$A = r_s^2 \arccos\left(\frac{d_1}{r_s}\right) - d_1\sqrt{r_s^2 - d_1^2} + r_m^2 \arccos\left(\frac{d_2}{r_m}\right) - d_1\sqrt{r_m^2 - d_2^2} \tag{B3}$$

where,

$$d_1 = \frac{r_s^2 - r_m^2 + \sqrt{d_0^2}}{2d_0} \tag{B4}$$

$$d_2 = d_0 - d_1 \tag{B5}$$

$$d_0 = \sqrt{x_m^2 - y_m^2} \tag{B6}$$

Acknowledgments

The study was supported by NSF-AGS 1929879 and NASA 80NSSC22K0324 to Boston University and the University of Colorado Boulder. PROBA2 Lyra data is available from https://proba2.sidc.be/data/lyra/level2. The ionosonde data is available from https://giro.uml.edu/didbase/scaled.php.

References

Aryal, S., Geddes, G., Finn, S. C., Mrak, S., Galkin, I., Cnossen, I., ... Chakrabarti, S. (2019, 5). Multispectral and multi-instrument observation of tids following

the total solar eclipse of 21 august 2017. *Journal of Geophysical Research: Space Physics*, *124*, 3761-3774. Retrieved from https://onlinelibrary.wiley.com/doi/abs/10.1029/2018JA026333 doi: 10.1029/2018JA026333

Barnes, W. T., Bobra, M. G., Christe, S. D., Freij, N., Hayes, L. A., Ireland, J., ... Dang, T. K. (2020). The sunpy project: Open source development and status of the version 1.0 core package. *The Astrophysical Journal*, *890*, 68. doi: 10.3847/1538-4357/ab4f7a

BenMoussa, A., Dammasch, I. E., Hochedez, J.-F., Schühle, U., Koller, S., Stockman, Y., ... Schmutz, W. (2009, 12). Pre-flight calibration of lyra, the solar vuv radiometer on board proba2. *Astronomy & Astrophysics*, *508*, 1085-1094. Retrieved from http://www.aanda.org/10.1051/0004-6361/200913089 doi: 10.1051/0004-6361/200913089

BenMoussa, A., Gissot, S., Schühle, U., Zanna, G. D., Auchère, F., Mekaoui, S., ... Woods, T. N. (2013, 11). On-orbit degradation of solar instruments. *Solar Physics*, *288*, 389-434. Retrieved from https://link.springer.com/article/10.1007/s11207-013-0290-z doi: 10.1007/S11207-013-0290-Z/FIGURES/27

Bravo, M., Martínez-Ledesma, M., Foppiano, A., Urra, B., Ovalle, E., Villalobos, C., ... Stepanova, M. (2020, 9). First report of an eclipse from chilean ionosonde observations: Comparison with total electron content estimations and the modeled maximum electron concentration and its height. *Journal of Geophysical Research: Space Physics*, *125*, 1-21. Retrieved from https://onlinelibrary.wiley.com/doi/10.1029/2020JA027923 doi: 10.1029/2020JA027923

Bullett, T., & Mabie, J. (2018, 4). Vertical and oblique ionosphere sounding during the 21 august 2017 solar eclipse. *Geophysical Research Letters*, *45*, 3690-3697. Retrieved from https://onlinelibrary.wiley.com/doi/abs/10.1002/2018GL077413 doi: 10.1002/2018GL077413

Chen, C.-H., Lin, C.-H. C., & Matsuo, T. (2019, 2). Ionospheric responses to the 21 august 2017 solar eclipse by using data assimilation approach. *Progress in Earth and Planetary Science*, *6*. Retrieved from https://progearthplanetsci.springeropen.com/articles/10.1186/s40645-019-0263-4http://files/1384/Chenetal.-2019-Ionosphericresponsestothe21August2017solar.pdf doi: 10.1186/s40645-019-0263-4

Cherniak, I., & Zakharenkova, I. (2018, 2). Ionospheric total electron content response to the great american solar eclipse of 21 august 2017. *Geophysical Research Letters*, *45*, 1199-1208. Retrieved from https://onlinelibrary.wiley.com/doi/10.1002/2017GL075989 doi: 10.1002/2017GL075989

Cnossen, I., Ridley, A. J., Goncharenko, L. P., & Harding, B. J. (2019, 8). The response of the ionosphere-thermosphere system to the 21 august 2017 solar eclipse. *Journal of Geophysical Research: Space Physics*, *124*, 7341-7355. Retrieved from https://onlinelibrary.wiley.com/doi/10.1029/2018JA026402 doi: 10.1029/2018JA026402

Coster, A. J., Goncharenko, L., Zhang, S.-R., Erickson, P. J., Rideout, W., & Vierinen, J. (2017, 12). Gnss observations of ionospheric variations during the 21 august 2017 solar eclipse. *Geophysical Research Letters*, *44*, 12,041-12,048. Retrieved from http://doi.wiley.com/10.1002/2017GL075774 doi: 10.1002/2017GL075774

Dang, T., Lei, J., Wang, W., Zhang, B., Burns, A., Le, H., ... Wan, W. (2018, 8). Global responses of the coupled thermosphere and ionosphere system to the august 2017 great american solar eclipse. *Journal of Geophysical Research: Space Physics*, *123*, 7040-7050. doi: 10.1029/2018JA025566

Darnel, J. M., Seaton, D. B., Bethge, C., Rachmeler, L., Jarvis, A., Hill, S. M., ... Timothy, S. (2022, 4). The goes-r solar ultraviolet imager. *Space Weather*,

20. Retrieved from https://onlinelibrary.wiley.com/doi/10.1029/2022SW003044 doi: 10.1029/2022SW003044

Davis, C. J., Lockwood, M., Bell, S. A., Smith, J. A., & Clarke, E. M. (2000, 2). Ionospheric measurements of relative coronal brightness during the total solar eclipses of 11 august, 1999 and 9 july, 1945. *Annales Geophysicae*, *18*, 182-190. Retrieved from https://angeo.copernicus.org/articles/18/182/2000/ doi: 10.1007/s00585-000-0182-z

Deehr, C. S., & Rees, M. H. (1964, 9). The eclipse of 20 july 1963 spectrophotometry of atmospheric emissions. *Planetary and Space Science*, *12*, 875-888. Retrieved from https://linkinghub.elsevier.com/retrieve/pii/0032063364900479 doi: 10.1016/0032-0633(64)90047-9

Deng, Y., Fuller-Rowell, T. J., Akmaev, R. A., & Ridley, A. J. (2011, 5). Impact of the altitudinal joule heating distribution on the thermosphere. *Journal of Geophysical Research: Space Physics*, *116*, 5313. Retrieved from http://doi.wiley.com/10.1029/2010JA016019 doi: 10.1029/2010JA016019

Deng, Y., Lin, C. Y., Zhu, Q., & Sheng, C. (2021, 3). *Influence of nonhydrostatic processes on the ionosphere-thermosphere* (Vol. 4). Retrieved from https://onlinelibrary.wiley.com/doi/10.1002/9781119815631.ch4 doi: 10.1002/9781119815631.ch4

Deng, Y., Richmond, A. D., Ridley, A. J., & Liu, H. L. (2008). Assessment of the non-hydrostatic effect on the upper atmosphere using a general circulation model (gcm). *Geophysical Research Letters*, *35*, 2-6. doi: 10.1029/2007GL032182

Dominique, M., Hochedez, J.-F., Schmutz, W., Dammasch, I. E., Shapiro, A. I., Kretzschmar, M., ... BenMoussa, A. (2013, 8). The lyra instrument onboard proba2: Description and in-flight performance. *Solar Physics*, *286*, 21-42. Retrieved from http://link.springer.com/10.1007/s11207-013-0252-5 doi: 10.1007/s11207-013-0252-5

Hairston, M. R., Mrak, S., Coley, W. R., Burrell, A., Holt, B., Perdue, M., ... Power, R. (2018, 8). Topside ionospheric electron temperature observations of the 21 august 2017 eclipse by dmsp spacecraft. *Geophysical Research Letters*, *45*, 7242-7247. Retrieved from http://doi.wiley.com/10.1029/2018GL077381 doi: 10.1029/2018GL077381

Harding, B. J., Drob, D. P., Buriti, R. A., & Makela, J. J. (2018, 4). Nightside detection of a large-scale thermospheric wave generated by a solar eclipse. *Geophysical Research Letters*, *45*, 3366-3373. Retrieved from https://onlinelibrary.wiley.com/doi/abs/10.1002/2018GL077015 doi: 10.1002/2018GL077015

He, L., Heki, K., & Wu, L. (2018). Three-dimensional and trans-hemispheric changes in ionospheric electron density caused by the great solar eclipse in north america on 21 august 2017. *Geophysical Research Letters*, *45*, 10,933-10,940. doi: 10.1029/2018GL080365

Huba, J. D., & Drob, D. (2017, 6). Sami3 prediction of the impact of the 21 august 2017 total solar eclipse on the ionosphere/plasmasphere system. *Geophysical Research Letters*, *44*, 5928-5935. Retrieved from http://doi.wiley.com/10.1002/2017GL073549 doi: 10.1002/2017GL073549

Kaplan, G. H., Bartlett, J. L., Monet, A. K. B., Bangert, J. A., & Puatua, W. K. (2011). *User's guide to novas version f3.1.*

Le, H., Liu, L., Yue, X., & Wan, W. (2008). The ionospheric responses to the 11 august 1999 solar eclipse: Observations and modeling. *Annales Geophysicae*, *26*, 107-116. doi: 10.5194/angeo-26-107-2008

Lemen, J. R., Title, A. M., Akin, D. J., Boerner, P. F., Chou, C., Drake, J. F., ... Waltham, N. (2012, 1). The atmospheric imaging assembly (aia) on the solar dynamics observatory (sdo). *Solar Physics*, *275*, 17-40. Retrieved from http://link.springer.com/10.1007/s11207-011-9776-8http://files/

1340/Lemenetal.-2012-TheAtmosphericImagingAssembly(AIA)ontheSola .pdf doi: 10.1007/s11207-011-9776-8

Lin, C. Y., Deng, Y., & Ridley, A. (2018, 5). Atmospheric gravity waves in the ionosphere and thermosphere during the 2017 solar eclipse. *Geophysical Research Letters*. Retrieved from http://doi.wiley.com/10.1029/2018GL077388http://files/857/Lin_et_al-2018-Geophysical_Research_Letters.pdf doi: 10.1029/2018GL077388

Lin, C. Y., Deng, Y., Sheng, C., & Drob, D. P. (2017, 1). A study of the nonlinear response of the upper atmosphere to episodic and stochastic acoustic-gravity wave forcing. *Journal of Geophysical Research: Space Physics*, *122*, 1178-1198. Retrieved from https://onlinelibrary.wiley.com/doi/10.1002/2016JA022930 doi: 10.1002/2016JA022930

Marriott, R. T., John, D. E. S., Thorne, R. M., & Venkateswaran, S. V. (1971, 12). Xuv image of the sun from eclipse observations of the ionospheric e-region. *Solar Physics*, *21*, 483-494. Retrieved from http://files/910/1971SoPh__21__483M.pdfhttp://link.springer.com/10.1007/BF00154303 doi: 10.1007/BF00154303

Marriott, R. T., John, D. E. S., Thorne, R. M., Venkateswaran, S. V., & Mahadevan, P. (1972). Ionospheric effects of two recent solar eclipses. *Journal of Atmospheric and Terrestrial Physics*, *34*, 695-712. doi: 10.1016/0021-9169(72)90157-2

Maute, A., & Richmond, A. D. (2017, 3). f-region dynamo simulations at low and mid-latitude. *Space Science Reviews*, *206*, 471-493. Retrieved from http://link.springer.com/10.1007/s11214-016-0262-3 doi: 10.1007/s11214-016-0262-3

McInerney, J. M., Marsh, D. R., Liu, H., Solomon, S. C., Conley, A. J., & Drob, D. P. (2018, 5). Simulation of the 21 august 2017 solar eclipse using the whole atmosphere community climate model-extended. *Geophysical Research Letters*, *45*, 3793-3800. Retrieved from https://onlinelibrary.wiley.com/doi/10.1029/2018GL077723 doi: 10.1029/2018GL077723

Meadows, P. (2007). The parallactic angle and the solar observer. *Journal of the British Astronomical Association*, *117*, 35-36.

Mrak, S. (2022, 09). *aldebaran1/pyeclipse: v0.1.0. [software].* Retrieved from https://github.com/aldebaran1/pyEclipse/ doi: 10.5281/zenodo.7044996

Mrak, S., Semeter, J., Drob, D., & Huba, J. D. (2018, 5). Direct euv/x-ray modulation of the ionosphere during the august 2017 total solar eclipse. *Geophysical Research Letters*, *45*, 3820-3828. Retrieved from http://doi.wiley.com/10.1029/2017GL076771 doi: 10.1029/2017GL076771

Nestorov, G., & Taubenheim, J. (1962, 7). Untersuchungen an der ionosphärischen e-schicht während der totalen sonnenfinsternis 15 februar 1961. *Journal of Atmospheric and Terrestrial Physics*, *24*, 633-642. Retrieved from https://linkinghub.elsevier.com/retrieve/pii/0021916962900855 doi: 10.1016/0021-9169(62)90085-5

Reinisch, B. W., Dandenault, P. B., Galkin, I. A., Hamel, R., & Richards, P. G. (2018, 2). Investigation of the electron density variation during the 21 august 2017 solar eclipse. *Geophysical Research Letters*, *45*, 1253-1261. Retrieved from https://onlinelibrary.wiley.com/doi/abs/10.1002/2017GL076572http://files/1371/Reinischetal.-2018-InvestigationoftheElectronDensityVariationDu.pdf doi: 10.1002/2017GL076572

Ridley, A., Deng, Y., & Tóth, G. (2006, 5). The global ionosphere–thermosphere model. *Journal of Atmospheric and Solar-Terrestrial Physics*, *68*, 839-864. Retrieved from https://linkinghub.elsevier.com/retrieve/pii/S1364682606000071 doi: 10.1016/j.jastp.2006.01.008

Ridley, E. C., Dickinson, R. E., Roble, R. G., & Rees, M. H. (1984, 9). Thermospheric response to the june 11, 1983, solar eclipse. *Journal of Geophysical Research: Space Physics*, *89*, 7583-7588. Retrieved from http://doi.wiley.com/10.1029/JA089iA09p07583 doi: 10.1029/JA089iA09p07583

Rishbeth, H. (1968, 9). Solar eclipses and ionospheric theory. *Space Science Reviews*, *8*, 543-554. Retrieved from http://link.springer.com/10.1007/BF00175006 doi: 10.1007/BF00175006

Smith, L. G., Accardo, C. A., Weeks, L. H., & McKinnon, P. J. (1965, 7). Measurements in the ionosphere during the solar eclipse of 20 july 1963. *Journal of Atmospheric and Terrestrial Physics*, *27*, 803-829. doi: 10.1016/0021-9169(65)90049-8

Stankov, S. M., Bergeot, N., Berghmans, D., Bolsée, D., Bruyninx, C., Chevalier, J.-M., ... West, M. J. (2017, 3). Multi-instrument observations of the solar eclipse on 20 march 2015 and its effects on the ionosphere over belgium and europe. *Journal of Space Weather and Space Climate*, *7*, A19. Retrieved from http://www.swsc-journal.org/10.1051/swsc/2017017http://files/799/swsc160032.pdf doi: 10.1051/swsc/2017017

Taubenheim, J., & Serafimov, K. (1969, 2). Brightness distribution of soft x-rays on the sun, inferred from ionospheric e-layer variations during an eclipse. *Journal of Atmospheric and Terrestrial Physics*, *31*, 307-312. Retrieved from https://linkinghub.elsevier.com/retrieve/pii/0021916969900476 doi: 10.1016/0021-9169(69)90047-6

Torr, D., Torr, M., Brinton, H., Brace, L., Spencer, N., Hedin, A., ... Rusch, D. (1979). An experimental and theoretical study of the mean diurnal variation of o ¡sup¿+¡/sup¿ , no ¡sup¿+¡/sup¿ , o ¡sub¿2¡/sub¿ ¡sup¿+¡/sup¿ , and n ¡sub¿2¡/sub¿ ¡sup¿+¡/sup¿ ions in the mid-latitude ¡i¿f¡/i¿ ¡sub¿1¡/sub¿ layer of the ionosphere. *Journal of Geophysical Research*, *84*, 3360. Retrieved from http://doi.wiley.com/10.1029/JA084iA07p03360 doi: 10.1029/JA084iA07p03360

Verhulst, T. G., & Stankov, S. M. (2018, 5). Ionospheric wave signature of the american solar eclipse on 21 august 2017 in europe. *Advances in Space Research*, *61*, 2245-2251. Retrieved from https://linkinghub.elsevier.com/retrieve/pii/S0273117718301224 doi: 10.1016/j.asr.2018.02.007

Verhulst, T. G. W., & Stankov, S. M. (2020, 7). Height dependency of solar eclipse effects: The ionospheric perspective. *Journal of Geophysical Research: Space Physics*, *125*, 1-20. Retrieved from https://onlinelibrary.wiley.com/doi/10.1029/2020JA028088 doi: 10.1029/2020JA028088

Wu, C., Ridley, A. J., Goncharenko, L., & Chen, G. (2018, 7). Gitm-data comparisons of the depletion and enhancement during the 2017 solar eclipse. *Geophysical Research Letters*, *45*, 3319-3327. Retrieved from http://doi.wiley.com/10.1002/2018GL077409http://files/963/2018GL077409.pdf doi: 10.1002/2018GL077409

Zhang, S. R., Erickson, P. J., Vierinen, J., Aa, E., Rideout, W., Coster, A. J., & Goncharenko, L. P. (2021, 2). Conjugate ionospheric perturbation during the 2017 solar eclipse. *Journal of Geophysical Research: Space Physics*, *126*. doi: 10.1029/2020JA028531

Zhu, Q., Deng, Y., Maute, A., Kilcommons, L. M., Knipp, D. J., & Hairston, M. (2021, 5). Ashley: A new empirical model for the high-latitude electron precipitation and electric field. *Space Weather*, *19*, 1-25. Retrieved from https://onlinelibrary.wiley.com/doi/10.1029/2020SW002671 doi: 10.1029/2020SW002671

Zhu, Q., Deng, Y., Maute, A., Sheng, C., & Lin, C. Y. (2017, 6). Impact of the vertical dynamics on the thermosphere at low and middle latitudes: Gitm simulations. *Journal of Geophysical Research: Space Physics*, *122*, 6882-6891. Retrieved from https://onlinelibrary.wiley.com/doi/10.1002/

2017JA023939 doi: 10.1002/2017JA023939

Zhu, Q., Deng, Y., Richmond, A., McGranaghan, R. M., & Maute, A. (2019, 5). Impacts of multiscale facs on the ionosphere-thermosphere system: Gitm simulation. *Journal of Geophysical Research: Space Physics*, *124*, 3532-3542. Retrieved from https://onlinelibrary.wiley.com/doi/10.1029/2018JA026082 doi: 10.1029/2018JA026082

Figure 1.

SUVI 171 Å 2021-12-04 08:28:31

AIA 171 Å 2021-12-04 08:30:09

Helioprojective Latitude (Solar-Y) [arcsec]

Helioprojective Longitude (Solar-X) [arcsec]

SDO AIA 171 A Eclipse

EOF=0.855

r_S

$1.1r_S$

local zenith

Solar N pole

η

Geometrically Symmetic Eclipse

Solar radius = $1.0r_S$

EOF=0.860

α

d

Figure 3.

Lusk, ID: 105.4W, 42.76N, 0km

2017-8-21

(a)

EOF

Time [UT]

geo--1.0
geo--1.1
AIA -- 94A
AIA -- 171A
AIA -- 193A
AIA -- 211A
AIA -- 304A

Iqaluit, Canada: 68.5W, 63.7N, 0km

2021-6-10

(b)

EOF

Time [UT]

geo--1.0
geo--1.1
AIA -- 94A
AIA -- 171A
AIA -- 193A
AIA -- 211A
AIA -- 304A

2021-6-10 9:10

EOF=0.914

(c)

2021-6-10 10:08

EOF=0.490

(d)

2021-6-10 11:15

EOF=0.981

(e)

Figure 4.

(a)

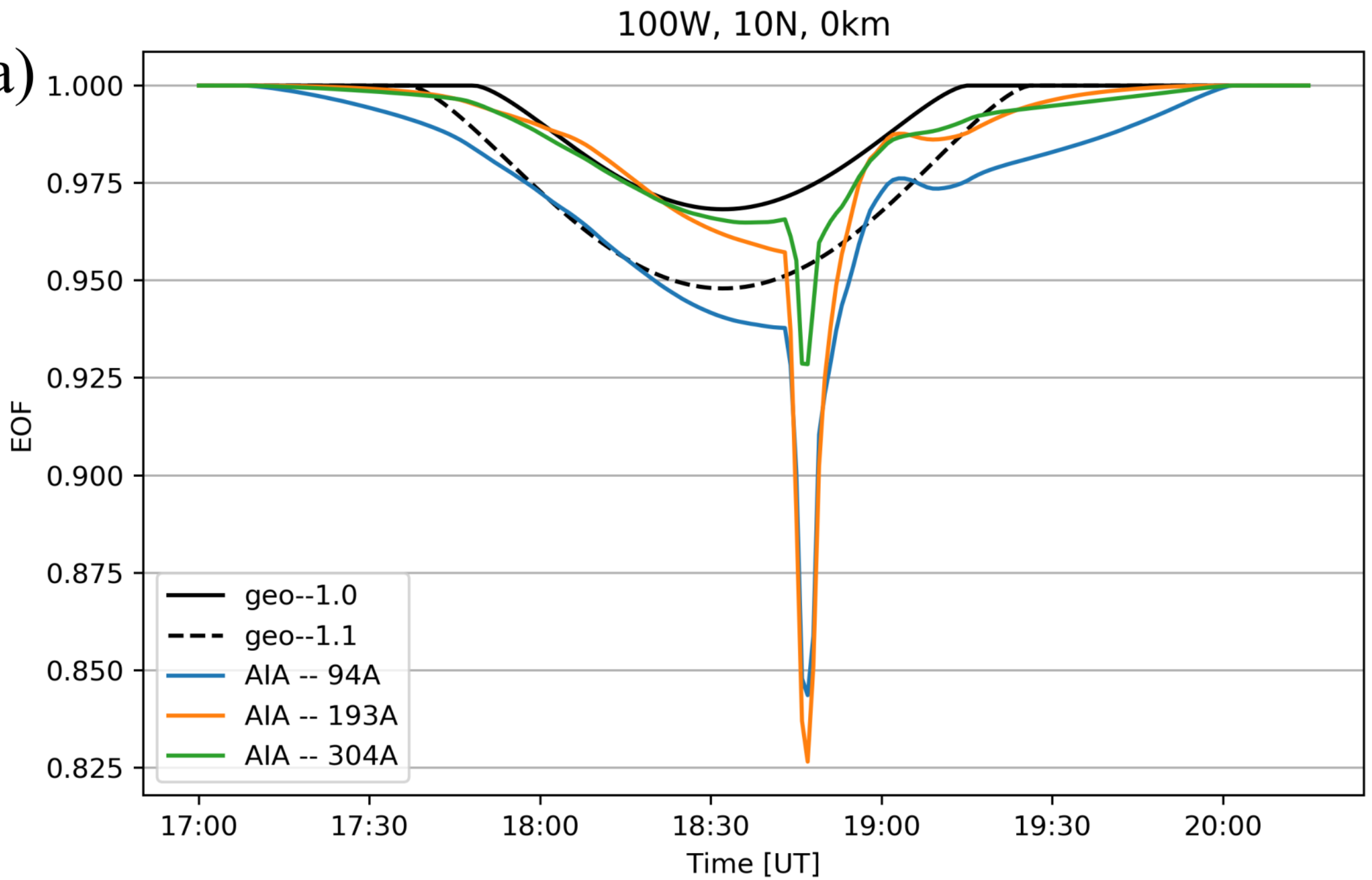
100W, 10N, 0km
1.000
0.975
0.950
0.925
0.900
0.875
0.850
0.825
EOF
geo--1.0
geo--1.1
AIA -- 94A
AIA -- 193A
AIA -- 304A
17:00
17:30
18:00
18:30
19:00
19:30
20:00
Time [UT]

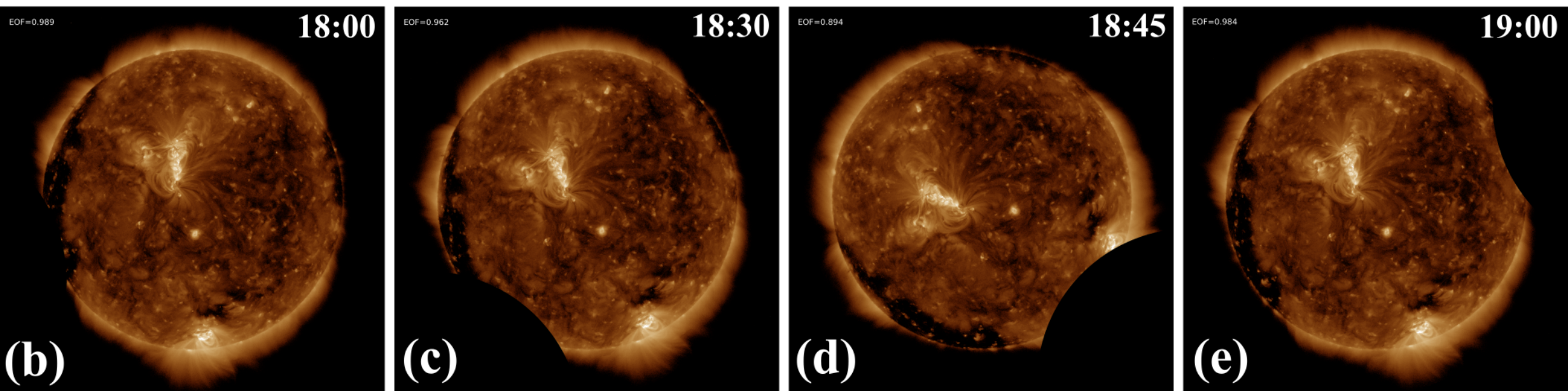
SDO AIA 193A
EOF=0.989
18:00
(b)
EOF=0.962
18:30
(c)
EOF=0.894
18:45
(d)
EOF=0.984
19:00
(e)

Figure 5.

(a) 2017-08-21 18:30:00, Alt = 150 km

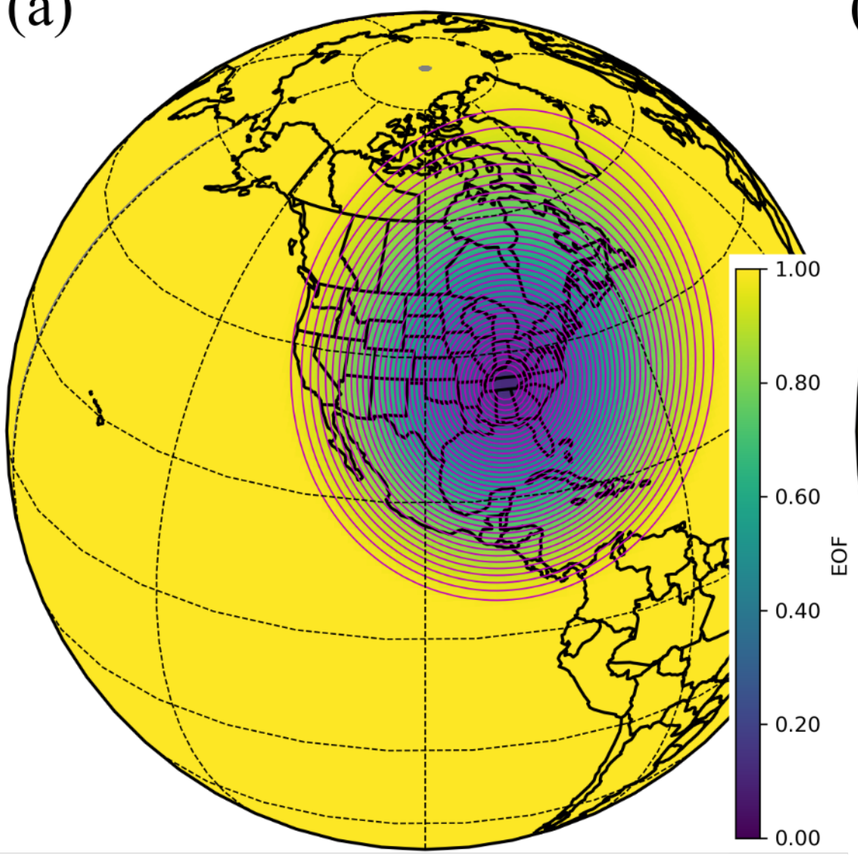

(b) 2017-08-21 18:30:00, Alt = 150 km

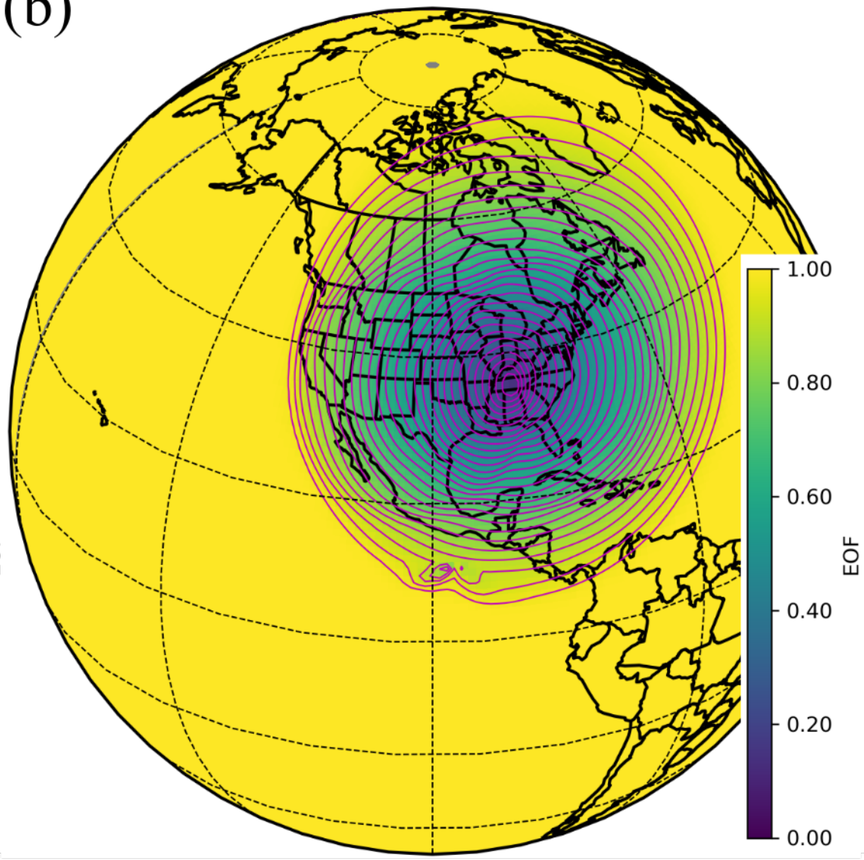

(c) 2017-08-21 18:30:00

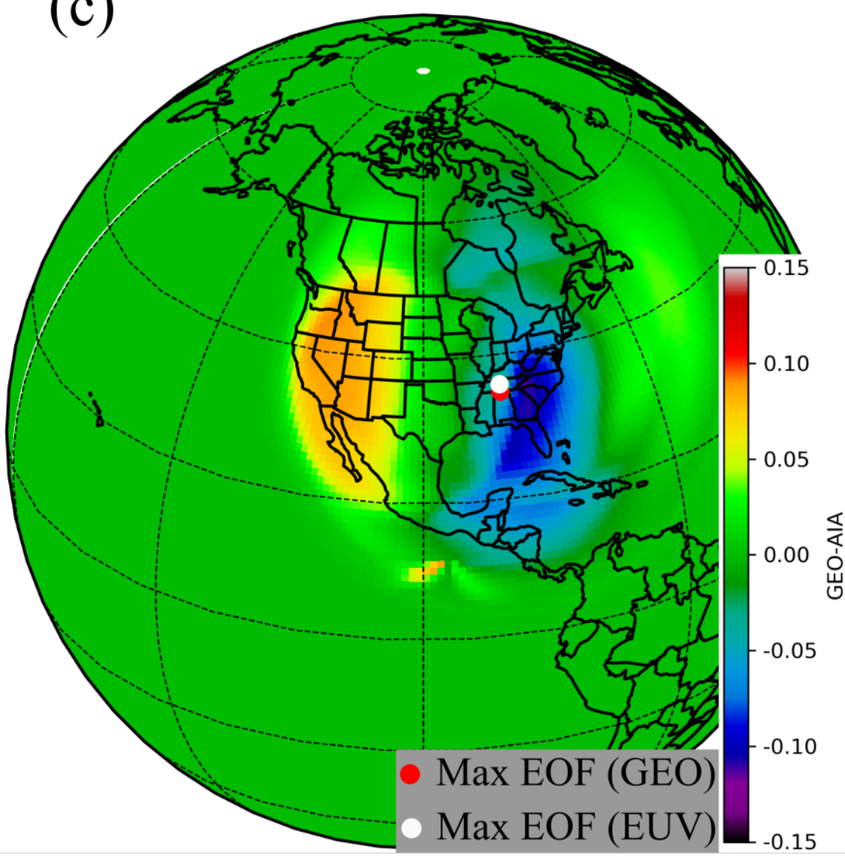

(d) 2021-06-10 10:00:00, Alt = 150 km

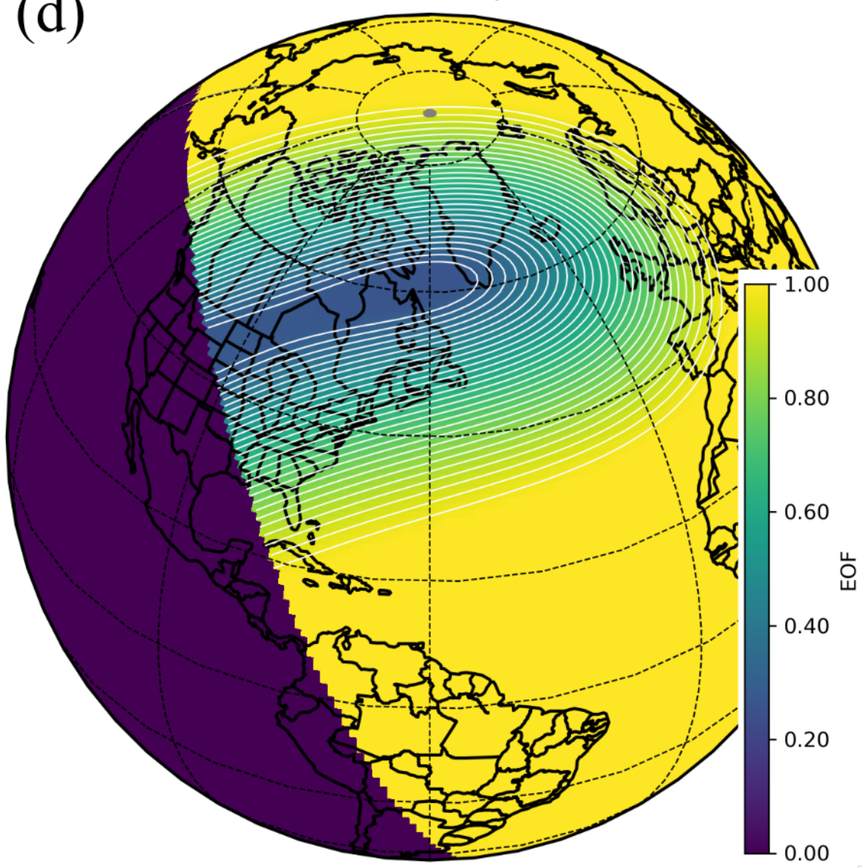

(e) 2021-06-10 10:00:00, Alt = 150 km

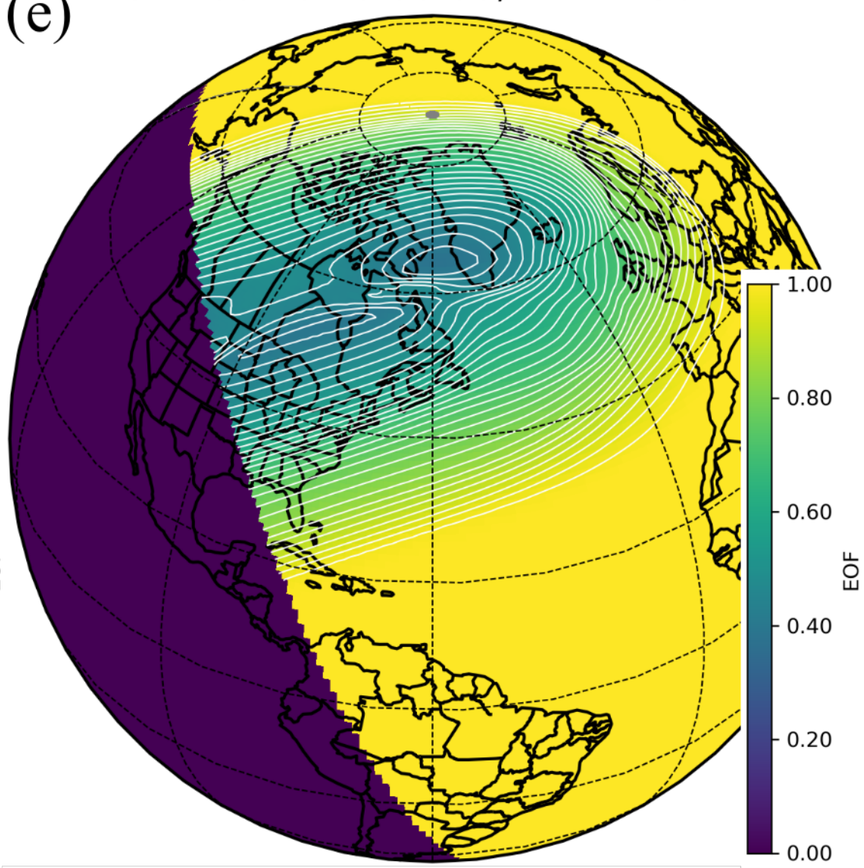

(f) 2021-06-10 10:00:00

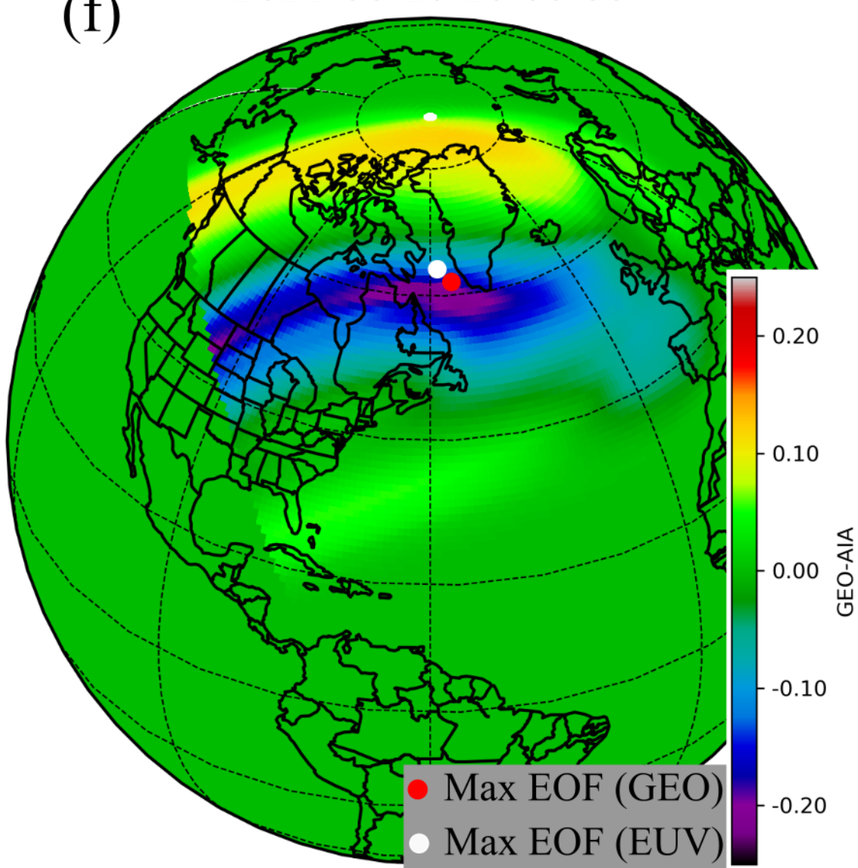

Figure 6.

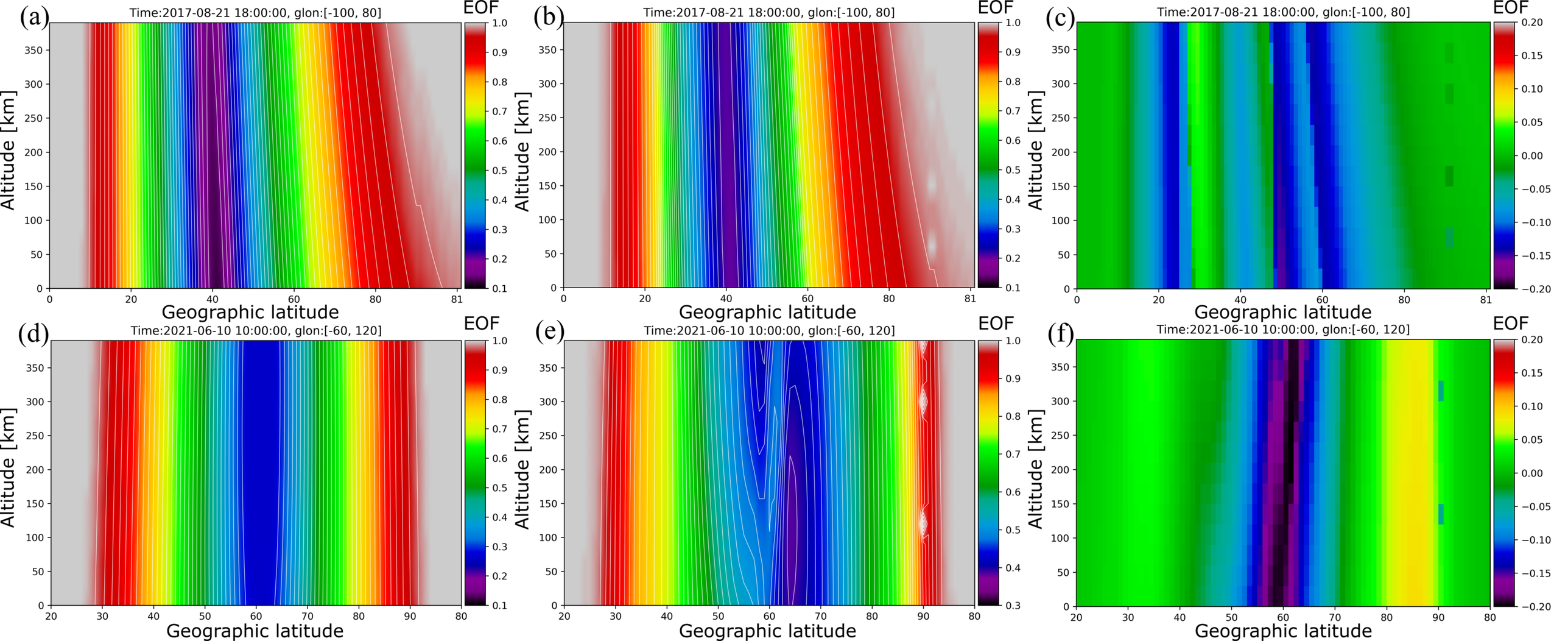
(a)
Time:2017-08-21 18:00:00, glon:[-100, 80]
EOF
Altitude [km]
Geographic latitude
(b)
Time:2017-08-21 18:00:00, glon:[-100, 80]
EOF
Altitude [km]
Geographic latitude
(c)
Time:2017-08-21 18:00:00, glon:[-100, 80]
EOF
Altitude [km]
Geographic latitude
(d)
Time:2021-06-10 10:00:00, glon:[-60, 120]
EOF
Altitude [km]
Geographic latitude
(e)
Time:2021-06-10 10:00:00, glon:[-60, 120]
EOF
Altitude [km]
Geographic latitude
(f)
Time:2021-06-10 10:00:00, glon:[-60, 120]
EOF
Altitude [km]
Geographic latitude

Figure 7.

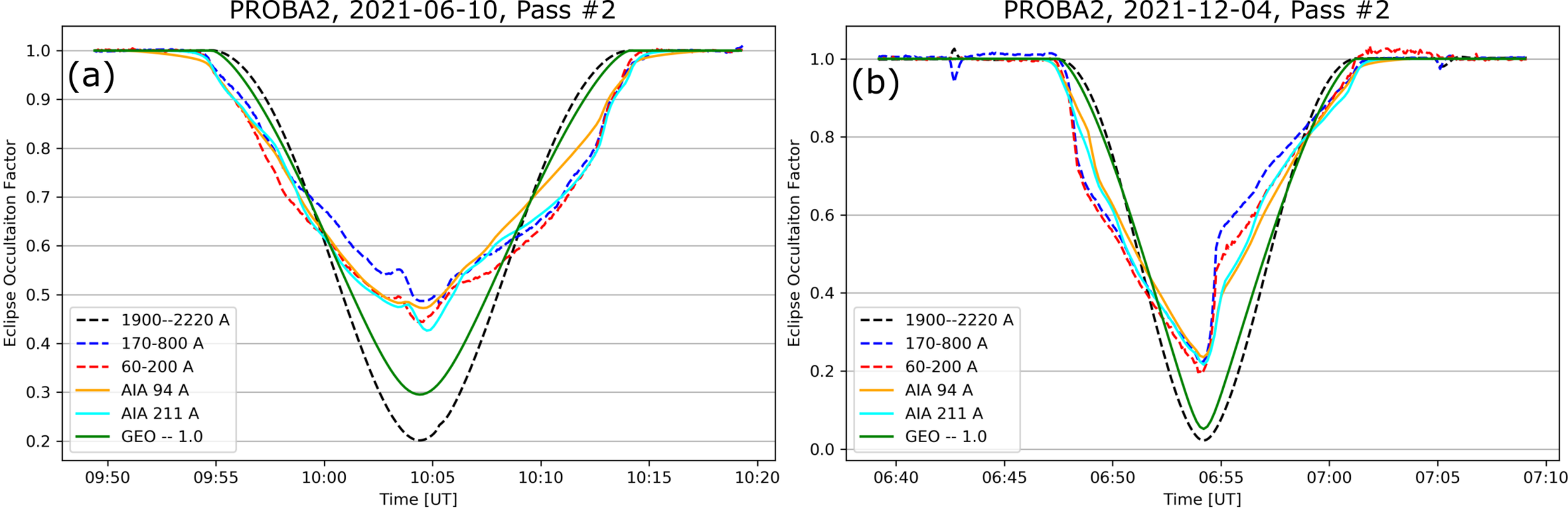
PROBA2, 2021-06-10, Pass #2
(a)
Eclipse Occultaiton Factor
1.0
0.9
0.8
0.7
0.6
0.5
0.4
0.3
0.2
1900--2220 A
170-800 A
60-200 A
AIA 94 A
AIA 211 A
GEO -- 1.0
09:50
09:55
10:00
10:05
10:10
10:15
10:20
Time [UT]
PROBA2, 2021-12-04, Pass #2
(b)
Eclipse Occultaiton Factor
1.0
0.8
0.6
0.4
0.2
0.0
1900--2220 A
170-800 A
60-200 A
AIA 94 A
AIA 211 A
GEO -- 1.0
06:40
06:45
06:50
06:55
07:00
07:05
07:10
Time [UT]

Figure 8.

(a)

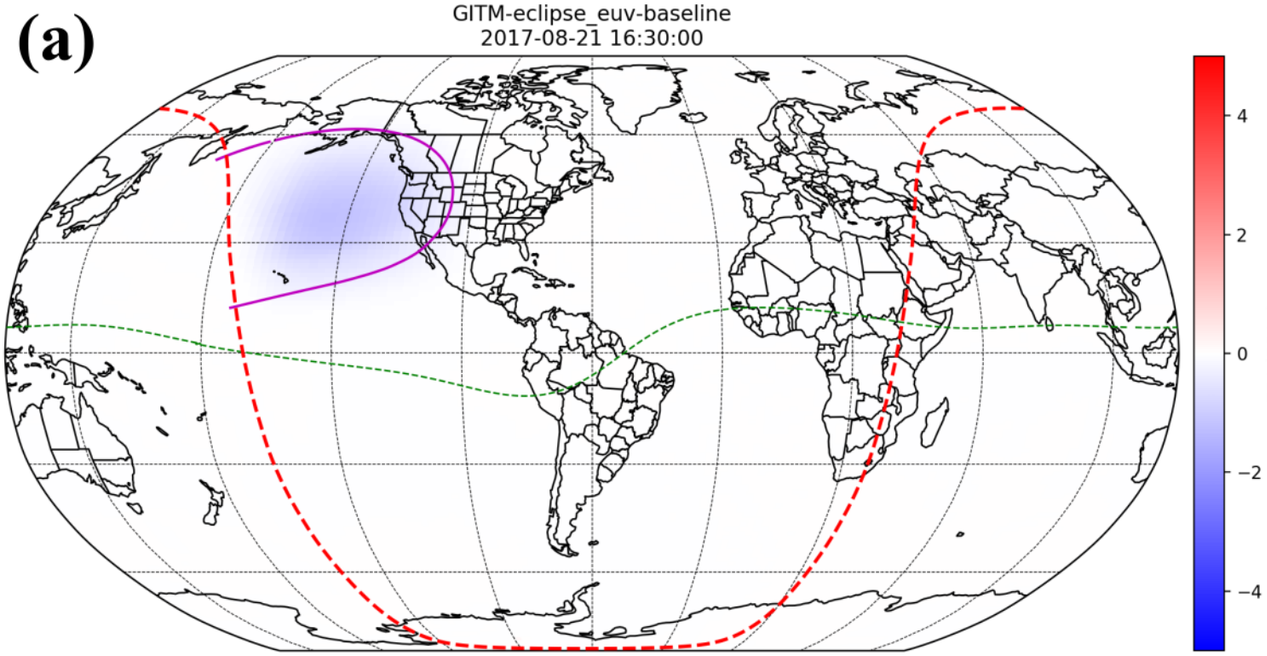
GITM-eclipse_euv-baseline
2017-08-21 16:30:00
TEC [TECu]
4
2
0
−2
−4

(b)

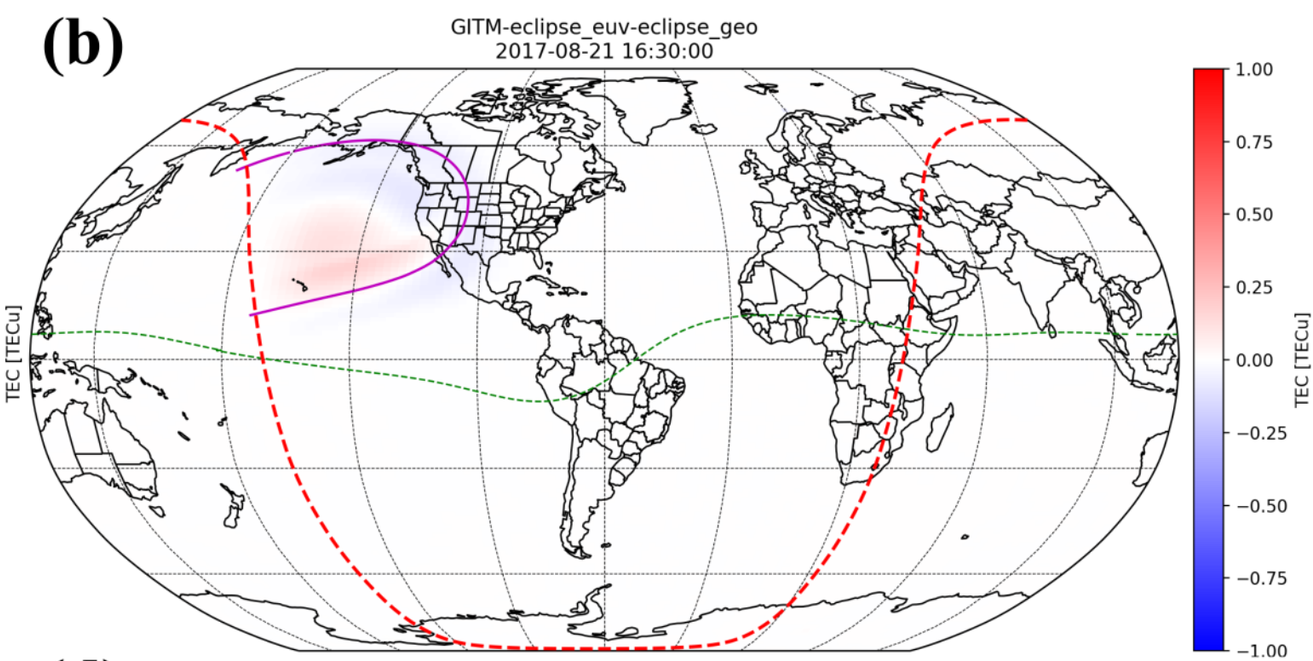
GITM-eclipse_euv-eclipse_geo
2017-08-21 16:30:00
TEC [TECu]
1.00
0.75
0.50
0.25
0.00
−0.25
−0.50
−0.75
−1.00

(c)

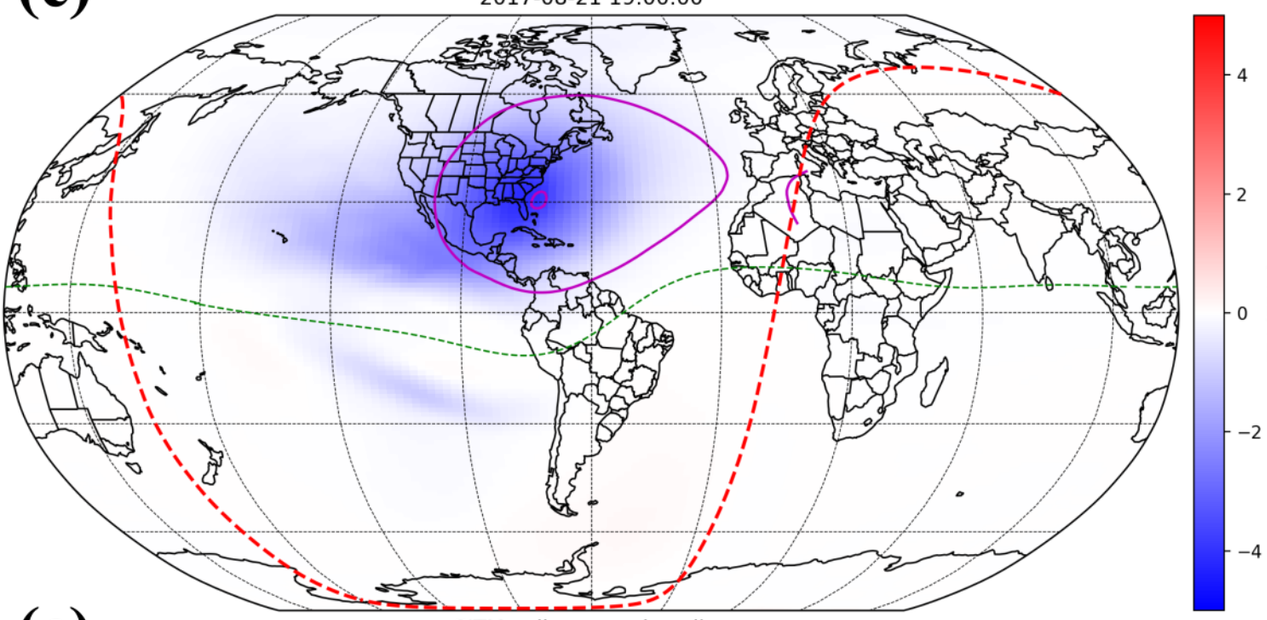
GITM-eclipse_euv-baseline
2017-08-21 19:00:00
TEC [TECu]
4
2
0
−2
−4

(d)

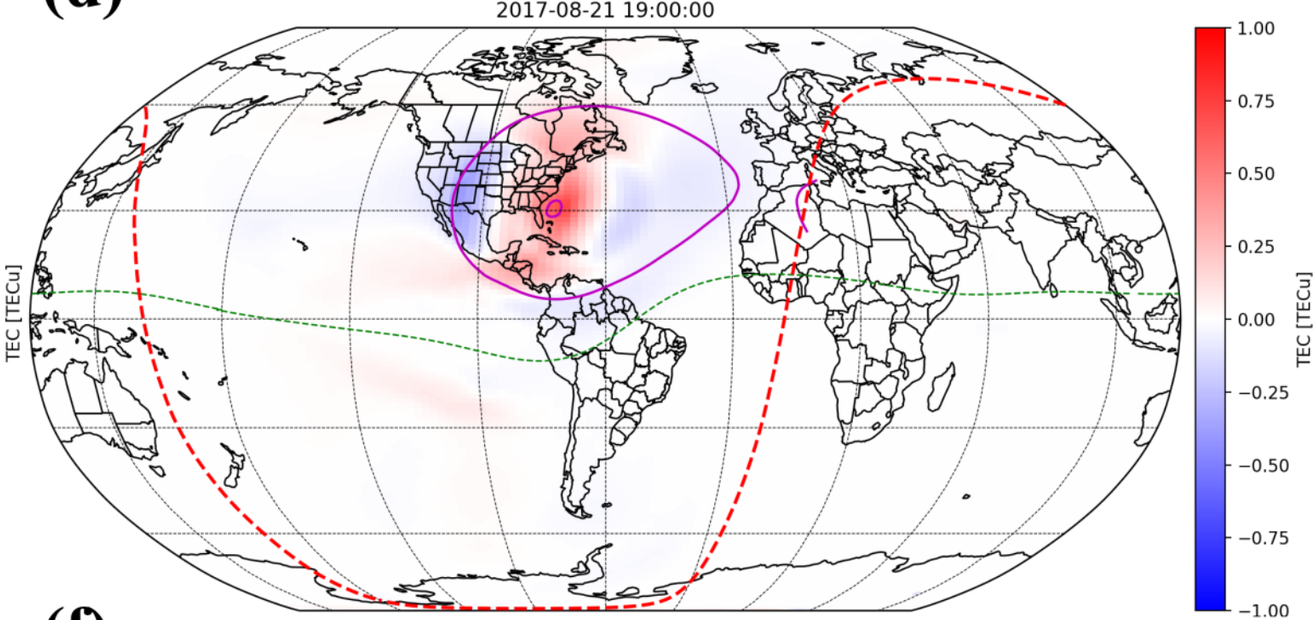
GITM-eclipse_euv-eclipse_geo
2017-08-21 19:00:00
TEC [TECu]
1.00
0.75
0.50
0.25
0.00
−0.25
−0.50
−0.75
−1.00

(e)

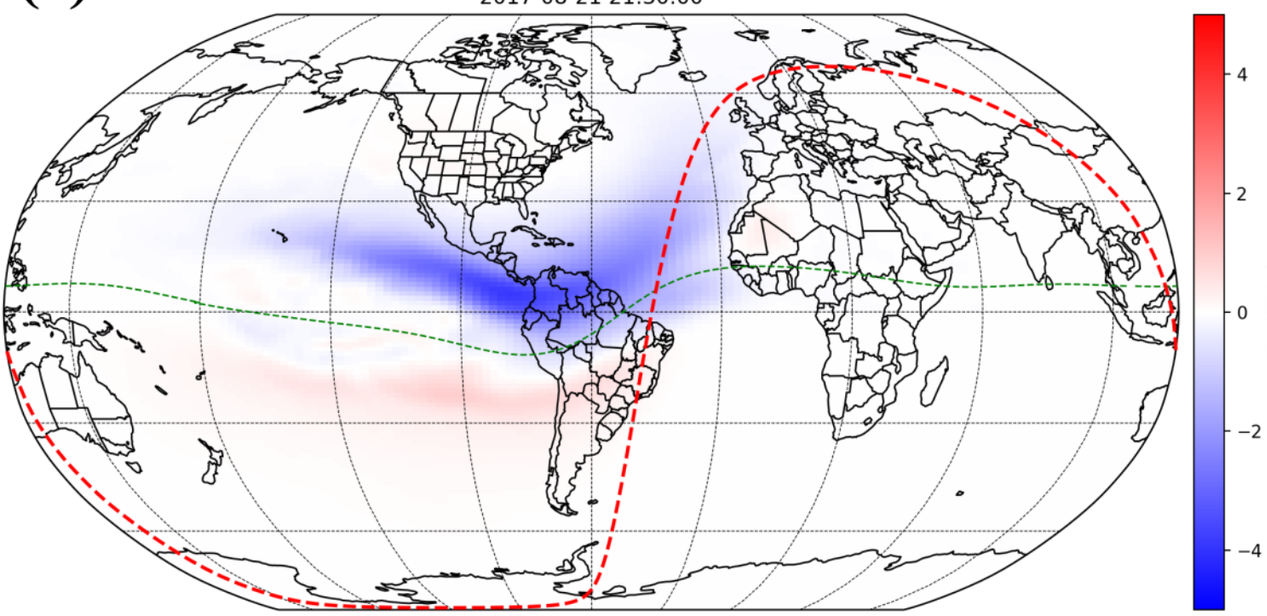
GITM-eclipse_euv-baseline
2017-08-21 21:30:00
TEC [TECu]
4
2
0
−2
−4

(f)

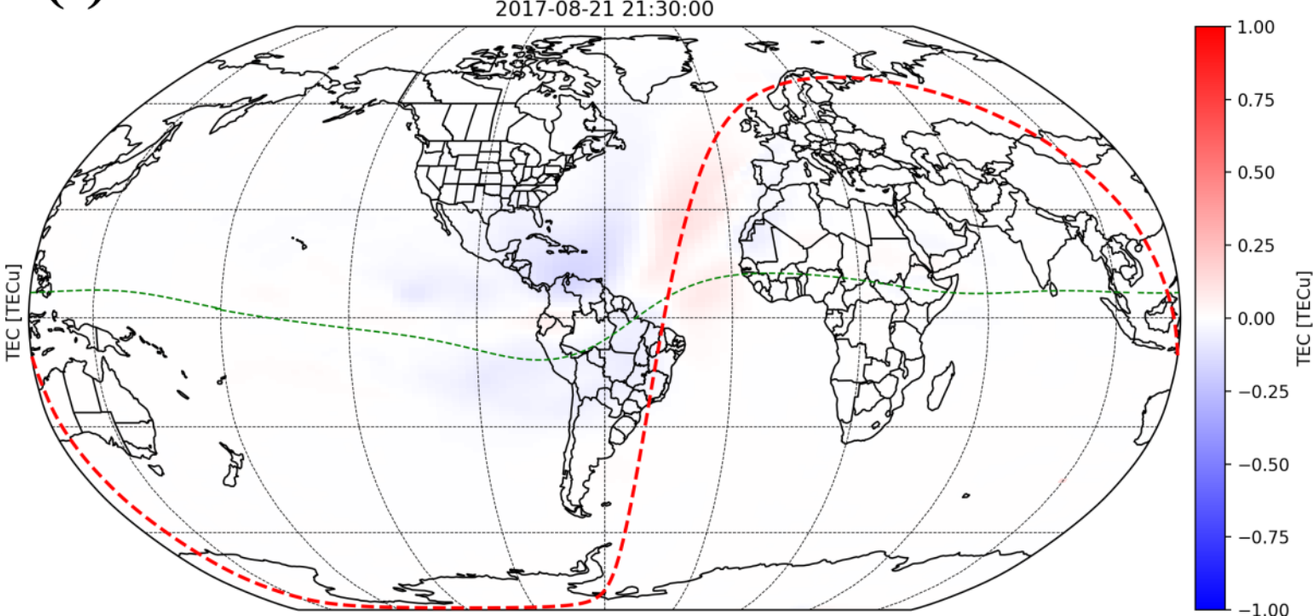
GITM-eclipse_euv-eclipse_geo
2017-08-21 21:30:00
TEC [TECu]
1.00
0.75
0.50
0.25
0.00
−0.25
−0.50
−0.75
−1.00

Figure 9.

(a)

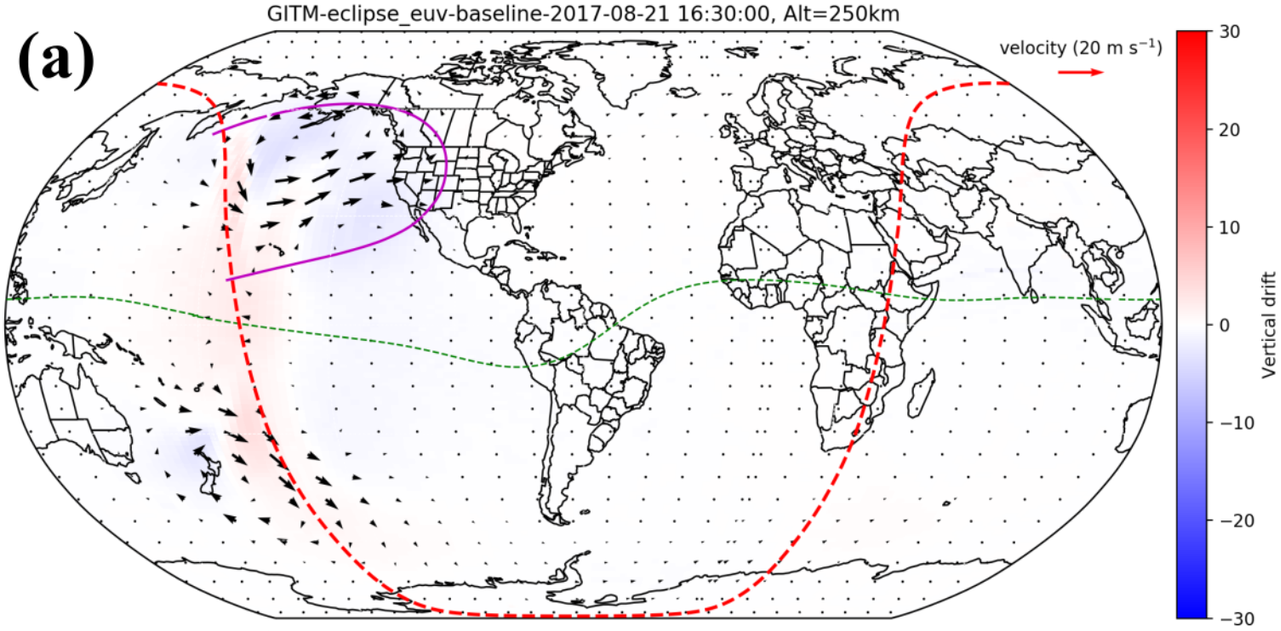
GITM-eclipse_euv-baseline-2017-08-21 16:30:00, Alt=250km
velocity (20 m s^{-1})
Vertical drift
30
20
10
0
−10
−20
−30

(b)

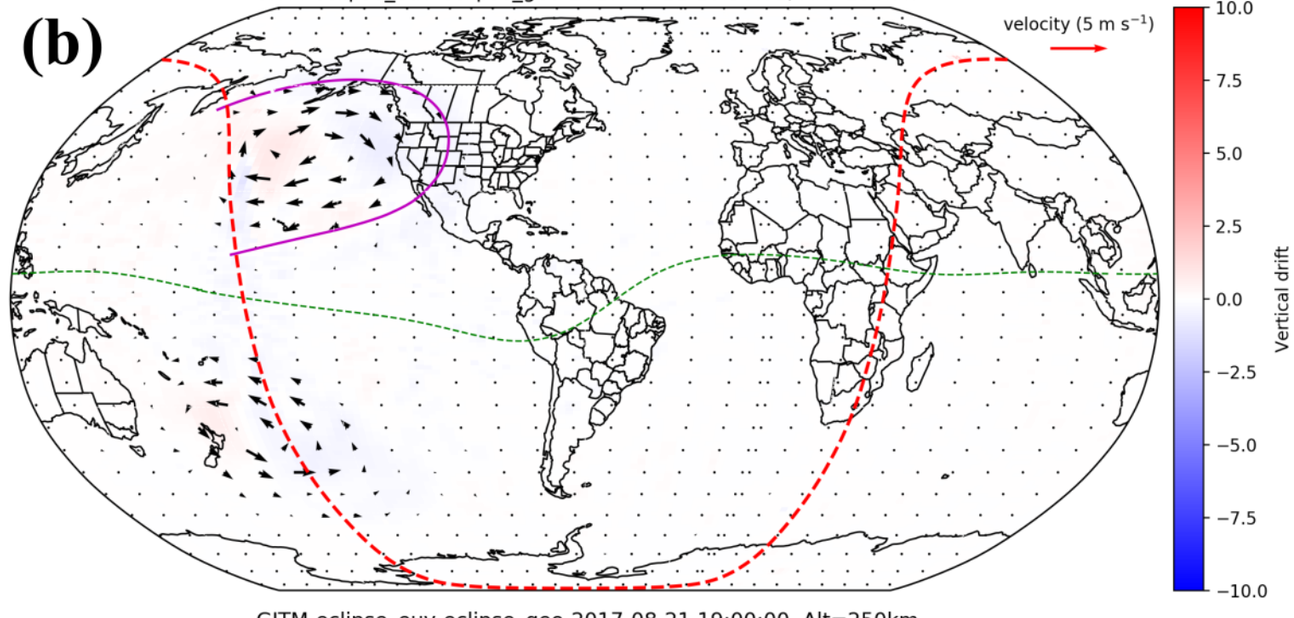
GITM-eclipse_euv-eclipse_geo-2017-08-21 16:30:01, Alt=250km
velocity (5 m s^{-1})
Vertical drift
10.0
7.5
5.0
2.5
0.0
−2.5
−5.0
−7.5
−10.0

(c)

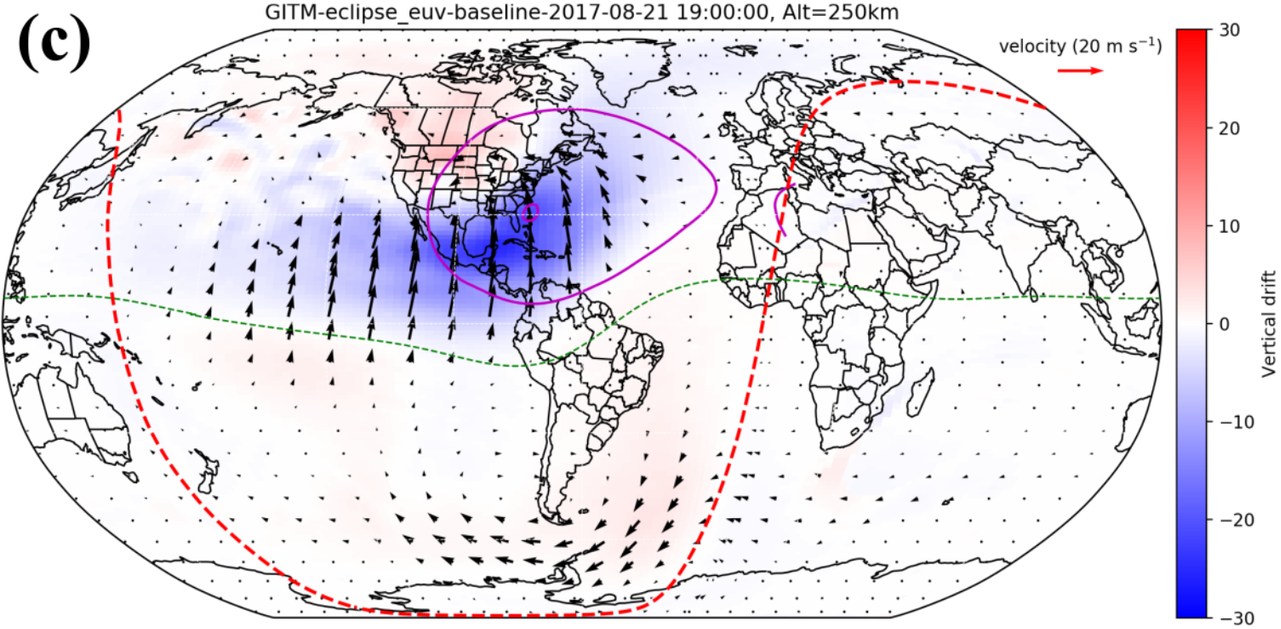
GITM-eclipse_euv-baseline-2017-08-21 19:00:00, Alt=250km
velocity (20 m s^{-1})
Vertical drift
30
20
10
0
−10
−20
−30

(d)

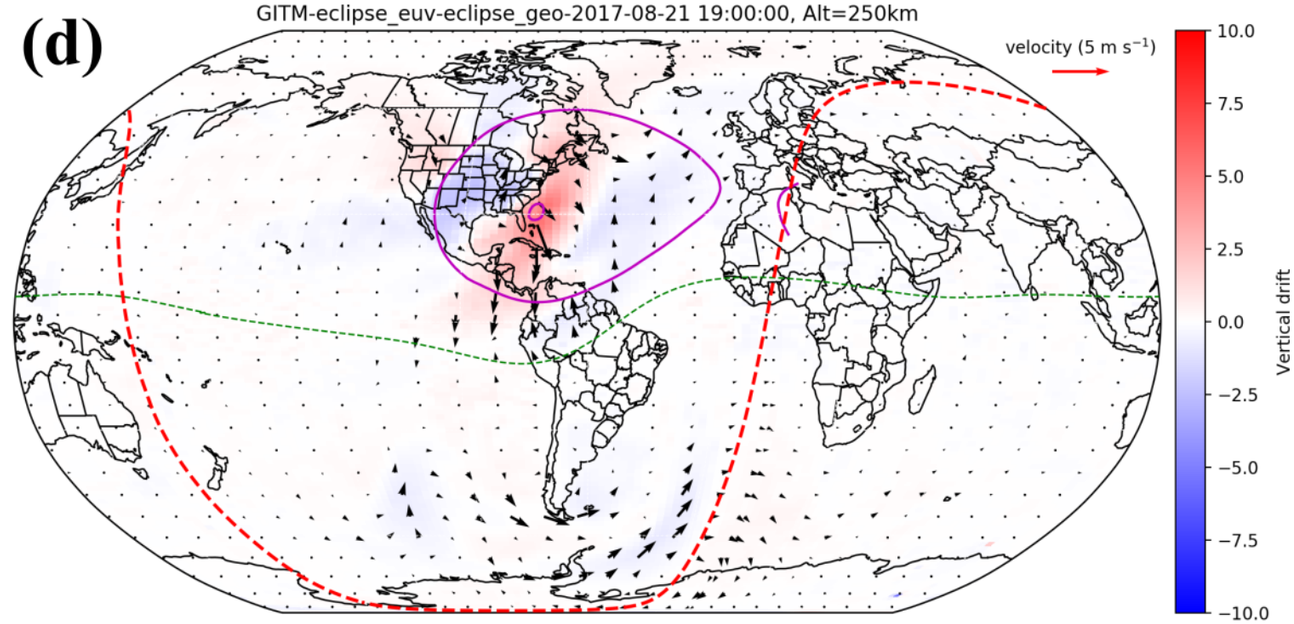
GITM-eclipse_euv-eclipse_geo-2017-08-21 19:00:00, Alt=250km
velocity (5 m s^{-1})
Vertical drift
10.0
7.5
5.0
2.5
0.0
−2.5
−5.0
−7.5
−10.0

(e)

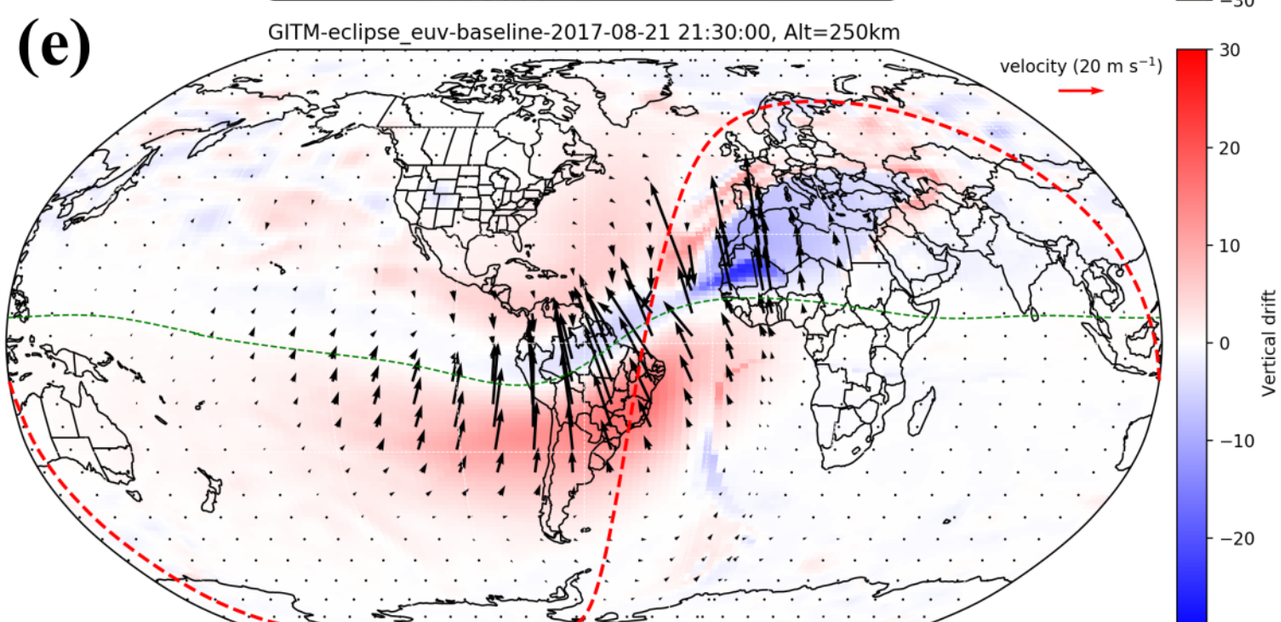
GITM-eclipse_euv-baseline-2017-08-21 21:30:00, Alt=250km
velocity (20 m s^{-1})
Vertical drift
30
20
10
0
−10
−20
−30

(f)

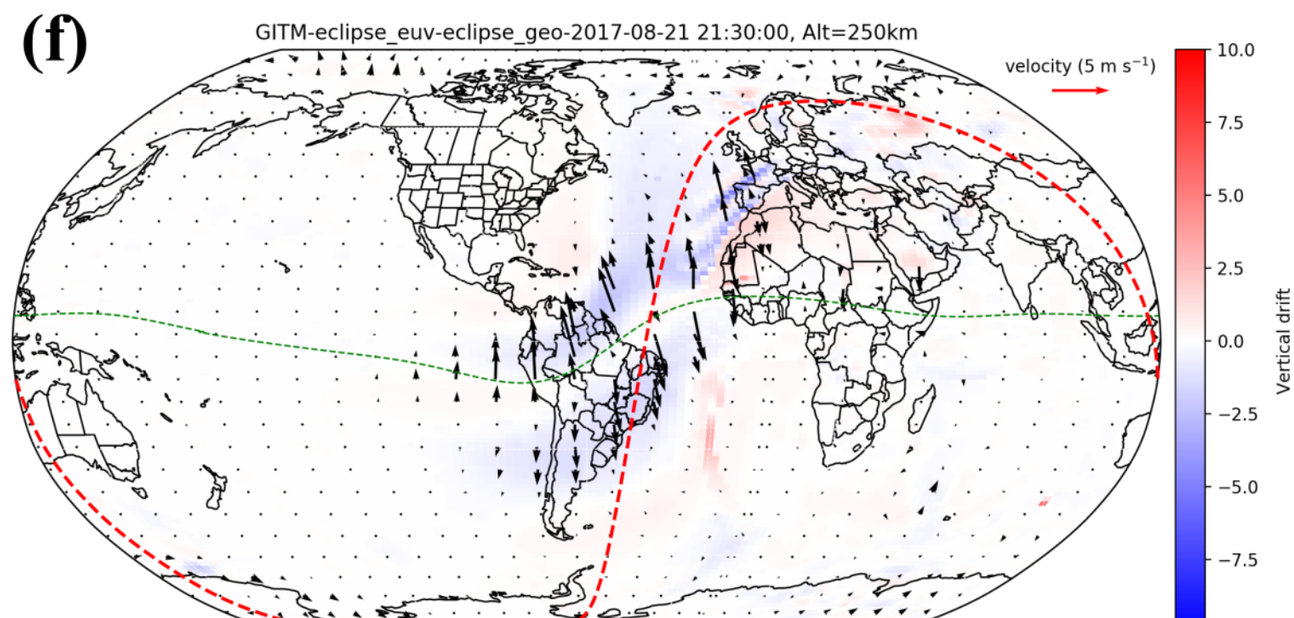
GITM-eclipse_euv-eclipse_geo-2017-08-21 21:30:00, Alt=250km
velocity (5 m s^{-1})
Vertical drift
10.0
7.5
5.0
2.5
0.0
−2.5
−5.0
−7.5
−10.0

Figure 10.

(a)

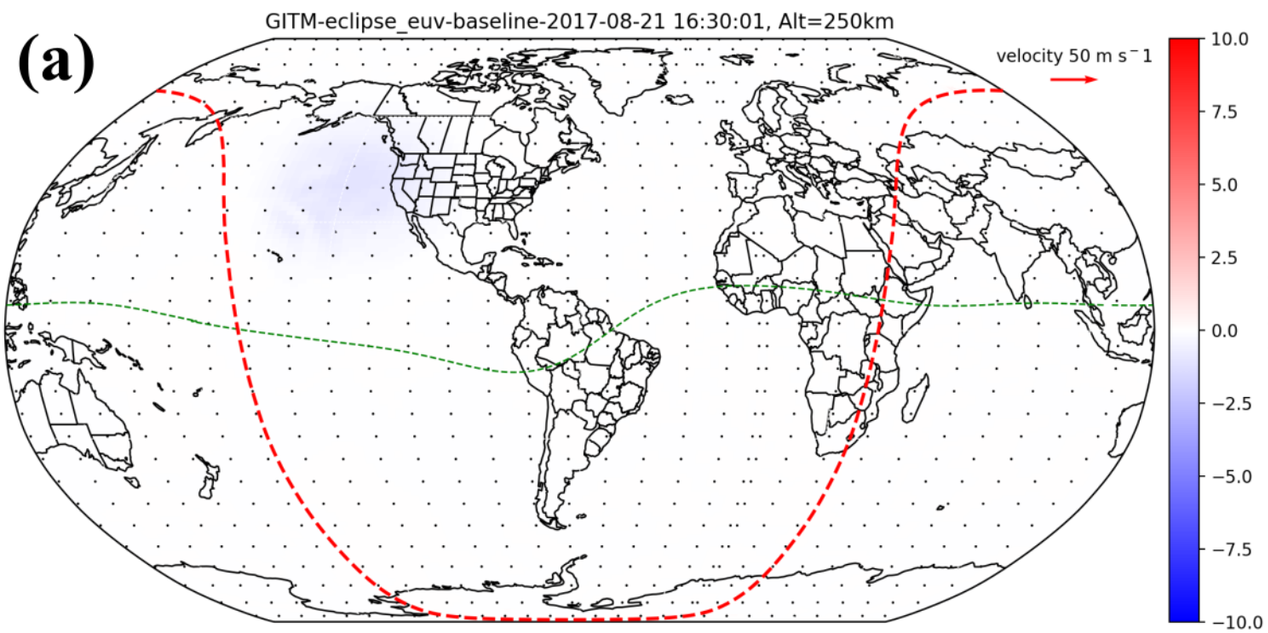
GITM-eclipse_euv-baseline-2017-08-21 16:30:01, Alt=250km
velocity 50 m s⁻1
10.0
7.5
5.0
2.5
0.0
−2.5
−5.0
−7.5
−10.0

(b)

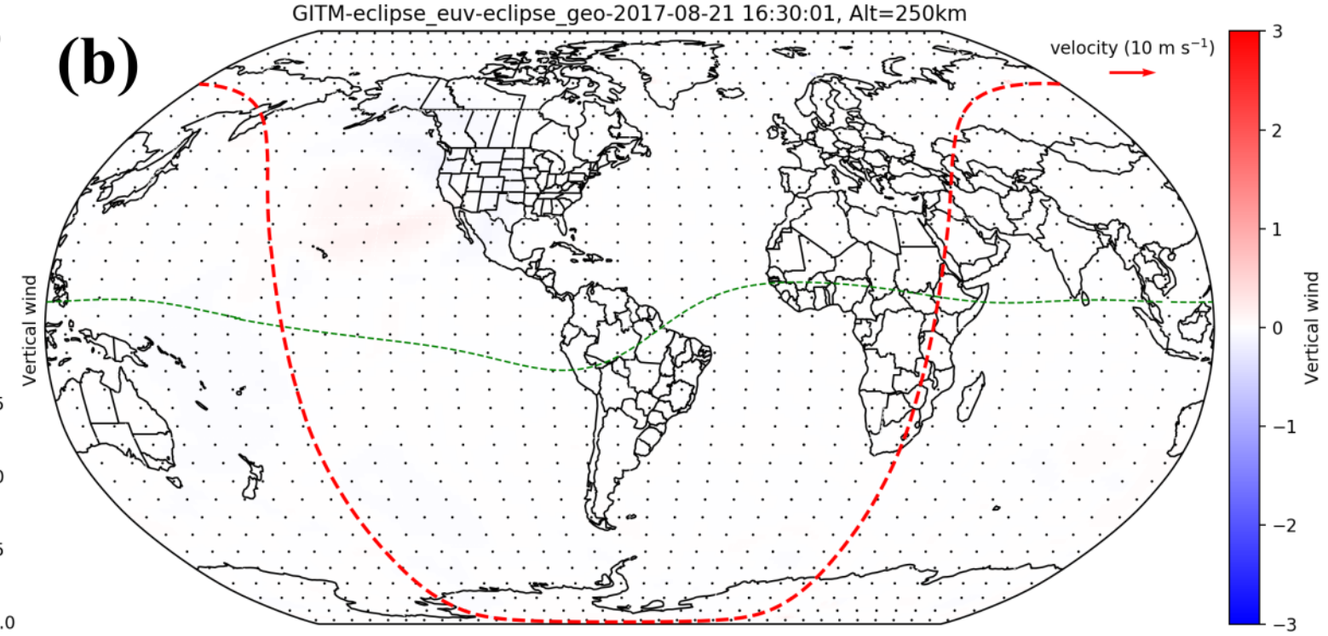
GITM-eclipse_euv-eclipse_geo-2017-08-21 16:30:01, Alt=250km
velocity (10 m s⁻¹)
Vertical wind
3
2
1
0
−1
−2
−3

(c)

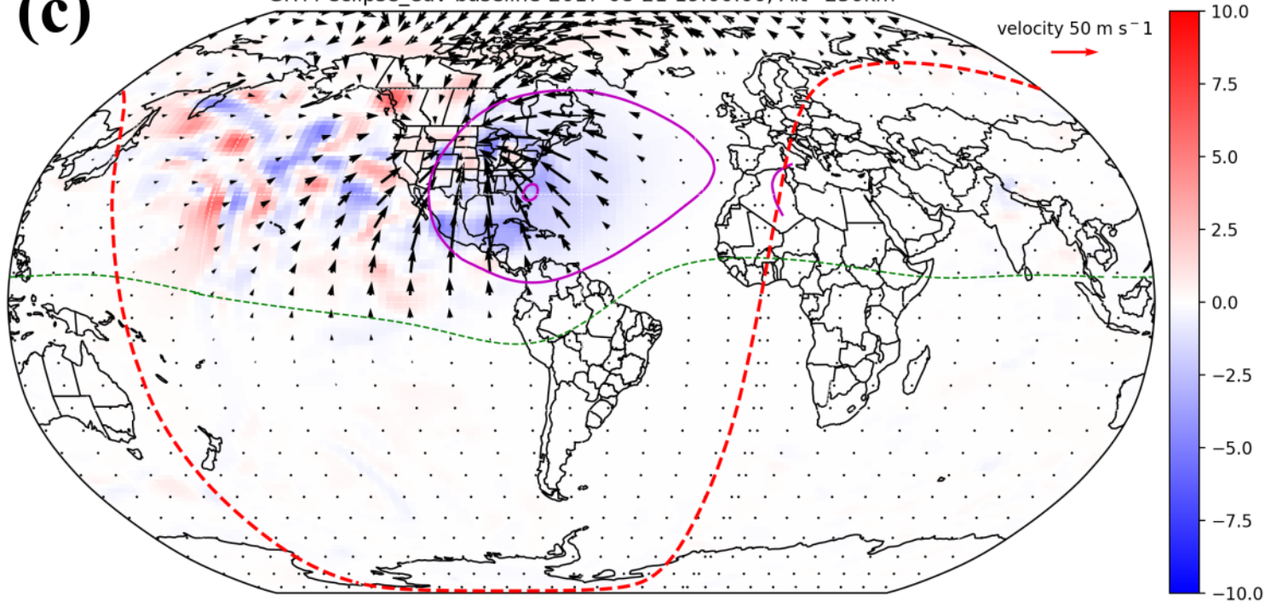
GITM-eclipse_euv-baseline-2017-08-21 19:00:00, Alt=250km
velocity 50 m s⁻1
10.0
7.5
5.0
2.5
0.0
−2.5
−5.0
−7.5
−10.0

(d)

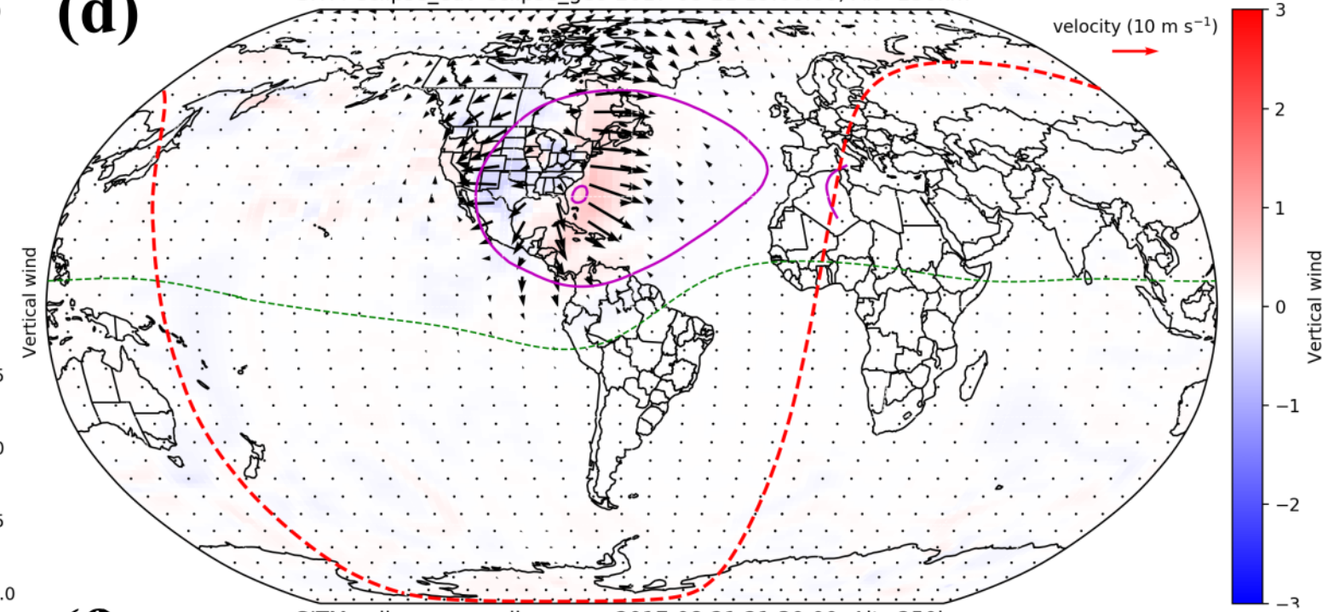
GITM-eclipse_euv-eclipse_geo-2017-08-21 19:00:00, Alt=250km
velocity (10 m s⁻¹)
Vertical wind
3
2
1
0
−1
−2
−3

(e)

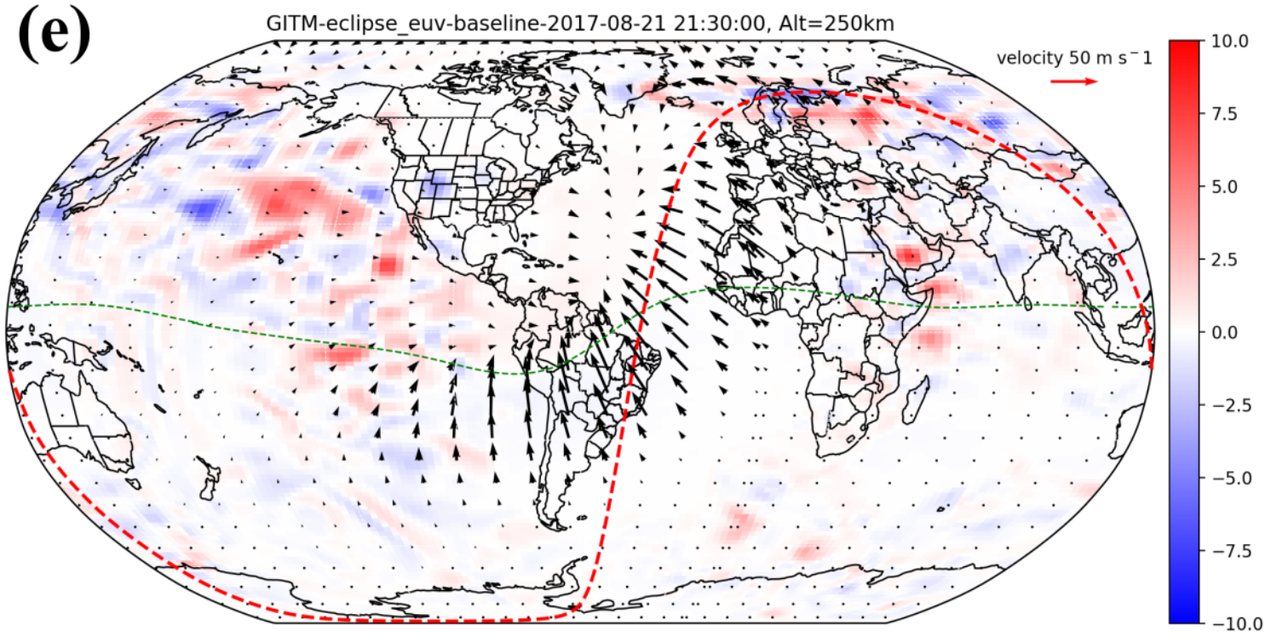
GITM-eclipse_euv-baseline-2017-08-21 21:30:00, Alt=250km
velocity 50 m s⁻1
10.0
7.5
5.0
2.5
0.0
−2.5
−5.0
−7.5
−10.0

(f)

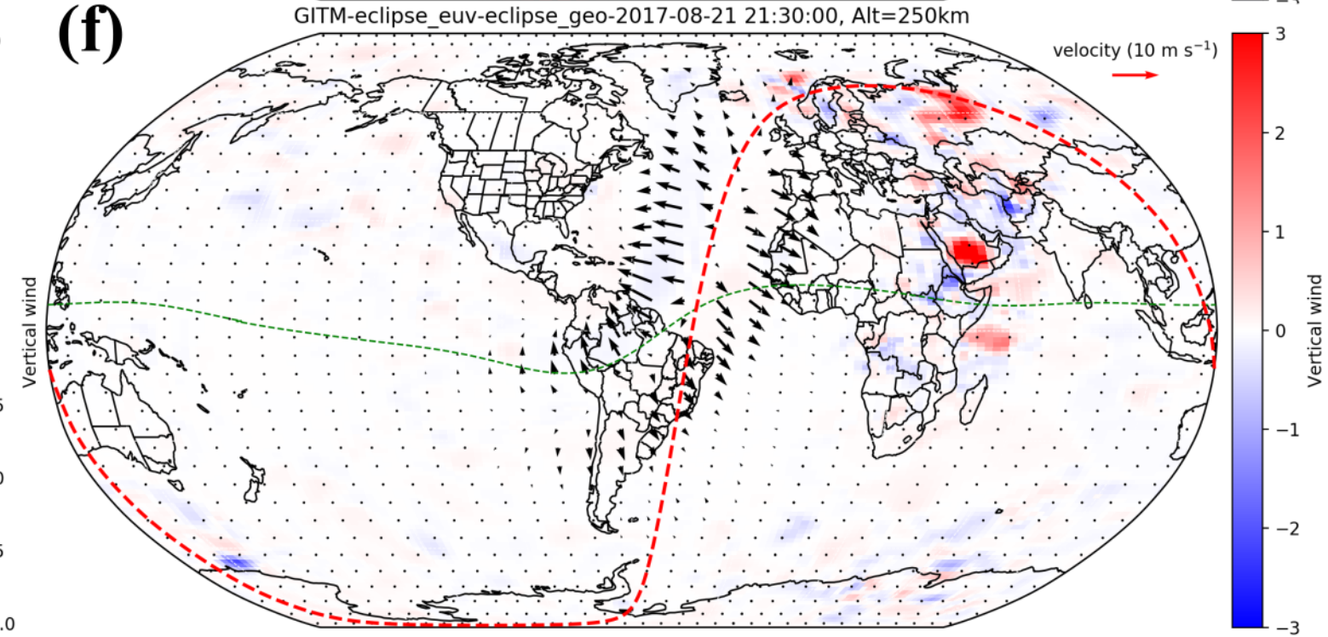
GITM-eclipse_euv-eclipse_geo-2017-08-21 21:30:00, Alt=250km
velocity (10 m s⁻¹)
Vertical wind
3
2
1
0
−1
−2
−3

Figure 11.

(a)

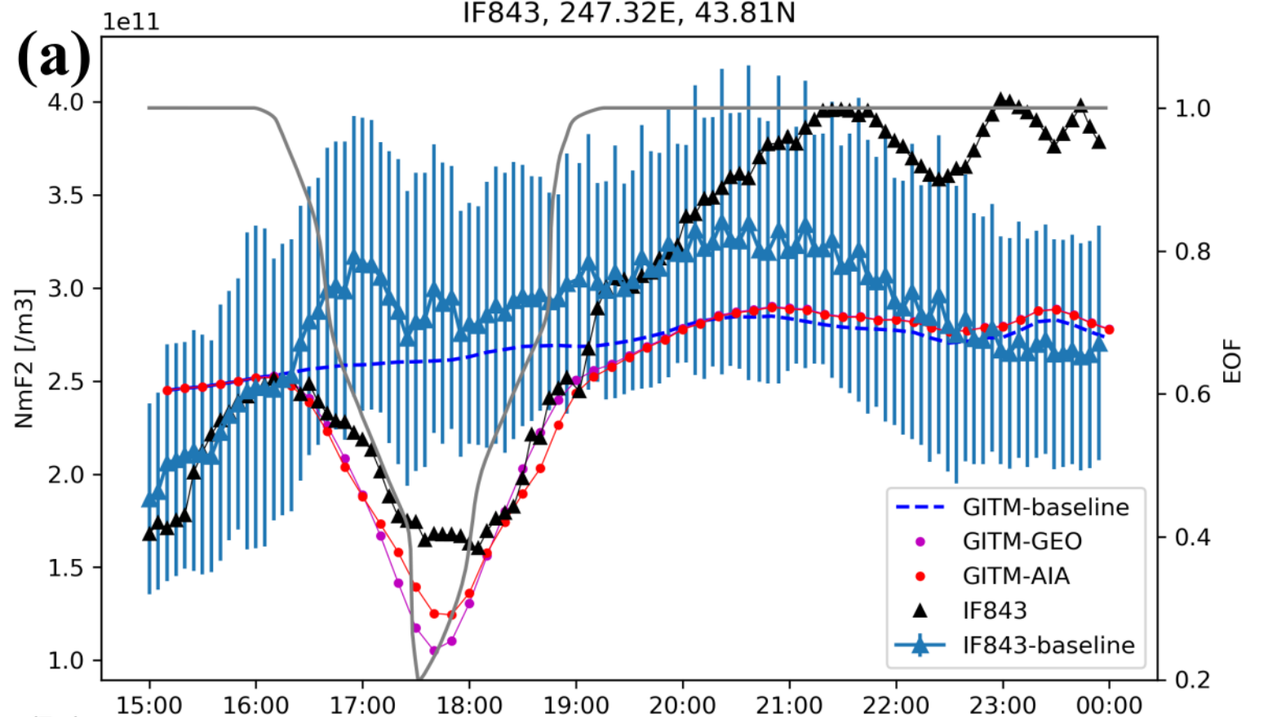
IF843, 247.32E, 43.81N
1e11
NmF2 [/m3]
EOF
GITM-baseline
GITM-GEO
GITM-AIA
IF843
IF843-baseline
15:00
16:00
17:00
18:00
19:00
20:00
21:00
22:00
23:00
00:00

(c)

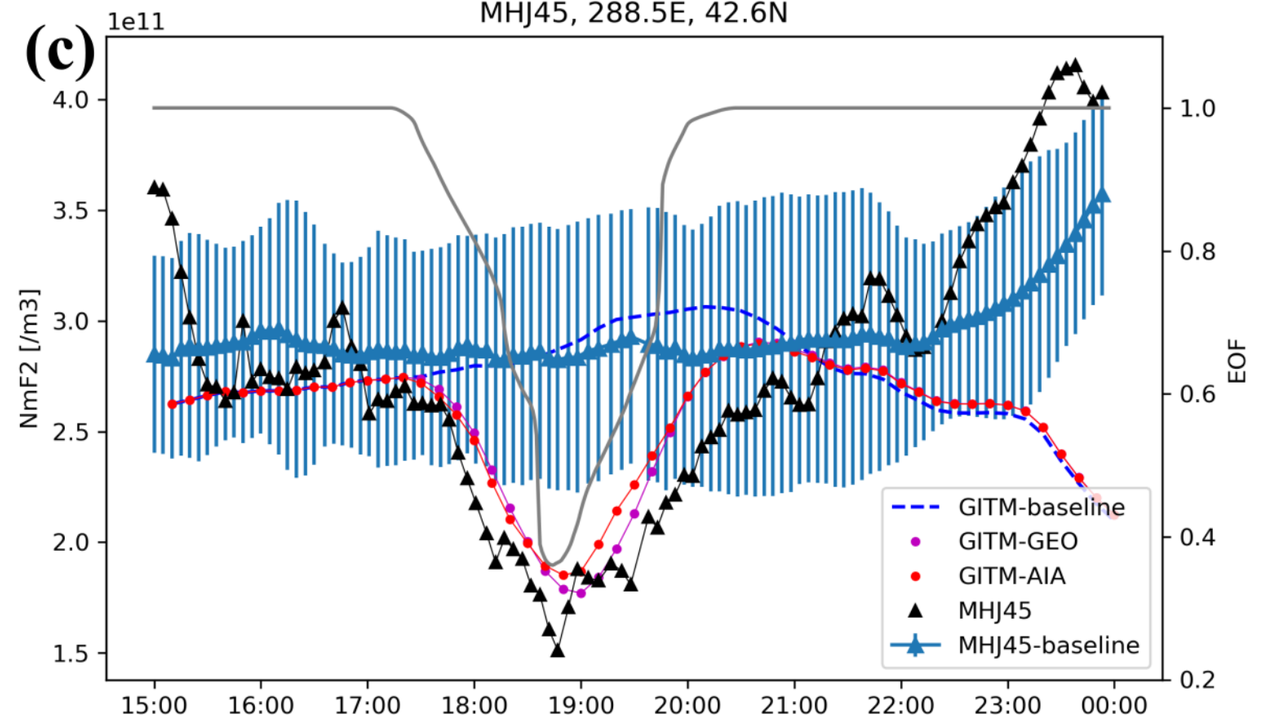
MHJ45, 288.5E, 42.6N
1e11
NmF2 [/m3]
EOF
GITM-baseline
GITM-GEO
GITM-AIA
MHJ45
MHJ45-baseline
15:00
16:00
17:00
18:00
19:00
20:00
21:00
22:00
23:00
00:00

(b)

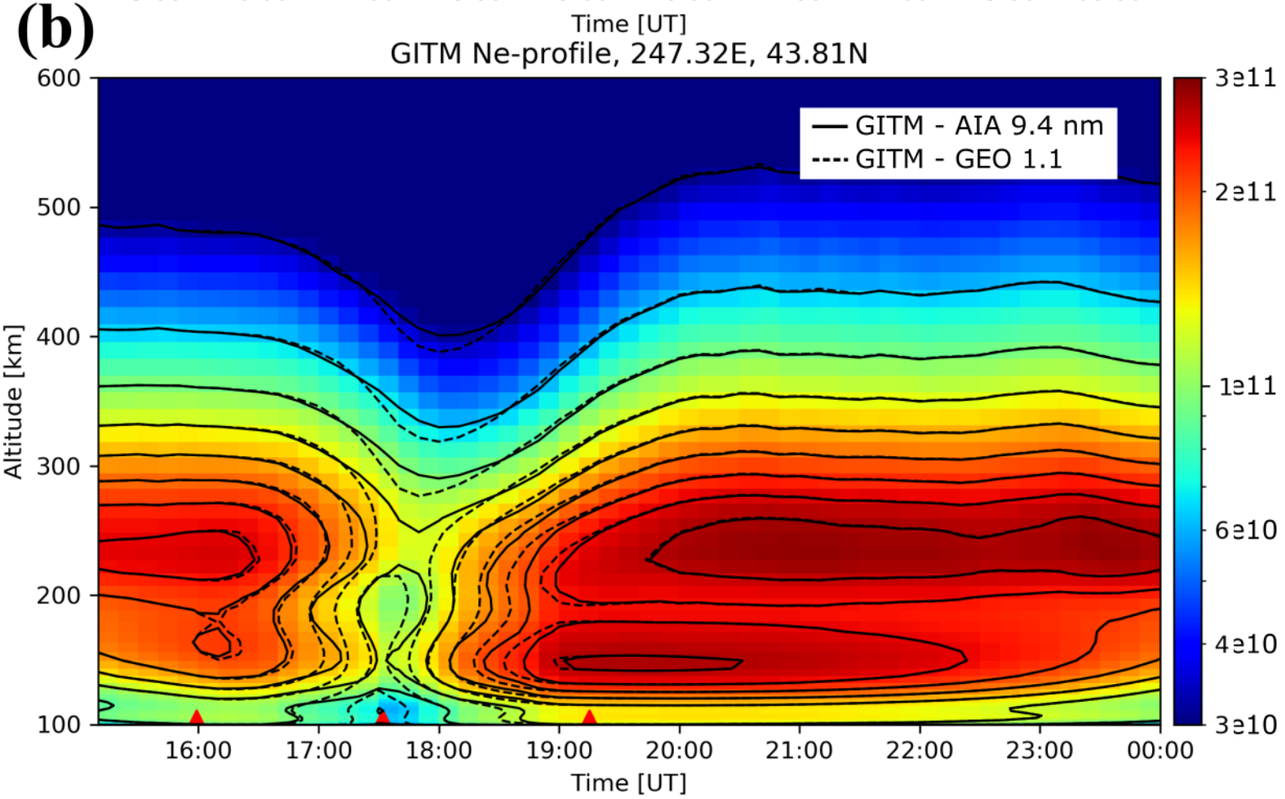
Time [UT]
GITM Ne-profile, 247.32E, 43.81N
GITM - AIA 9.4 nm
GITM - GEO 1.1
Altitude [km]
Time [UT]
16:00
17:00
18:00
19:00
20:00
21:00
22:00
23:00
00:00

(d)

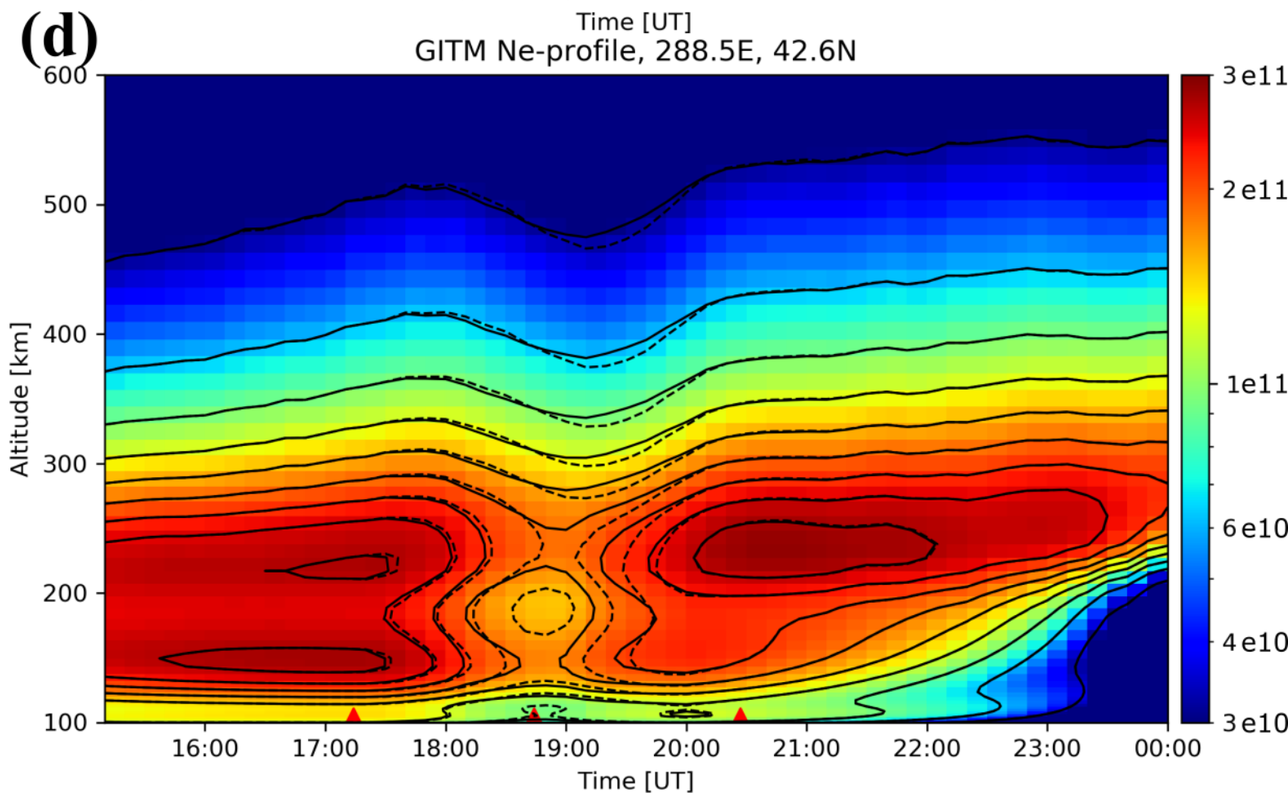
Time [UT]
GITM Ne-profile, 288.5E, 42.6N
Altitude [km]
Time [UT]
16:00
17:00
18:00
19:00
20:00
21:00
22:00
23:00
00:00

Figure A1.

(a)

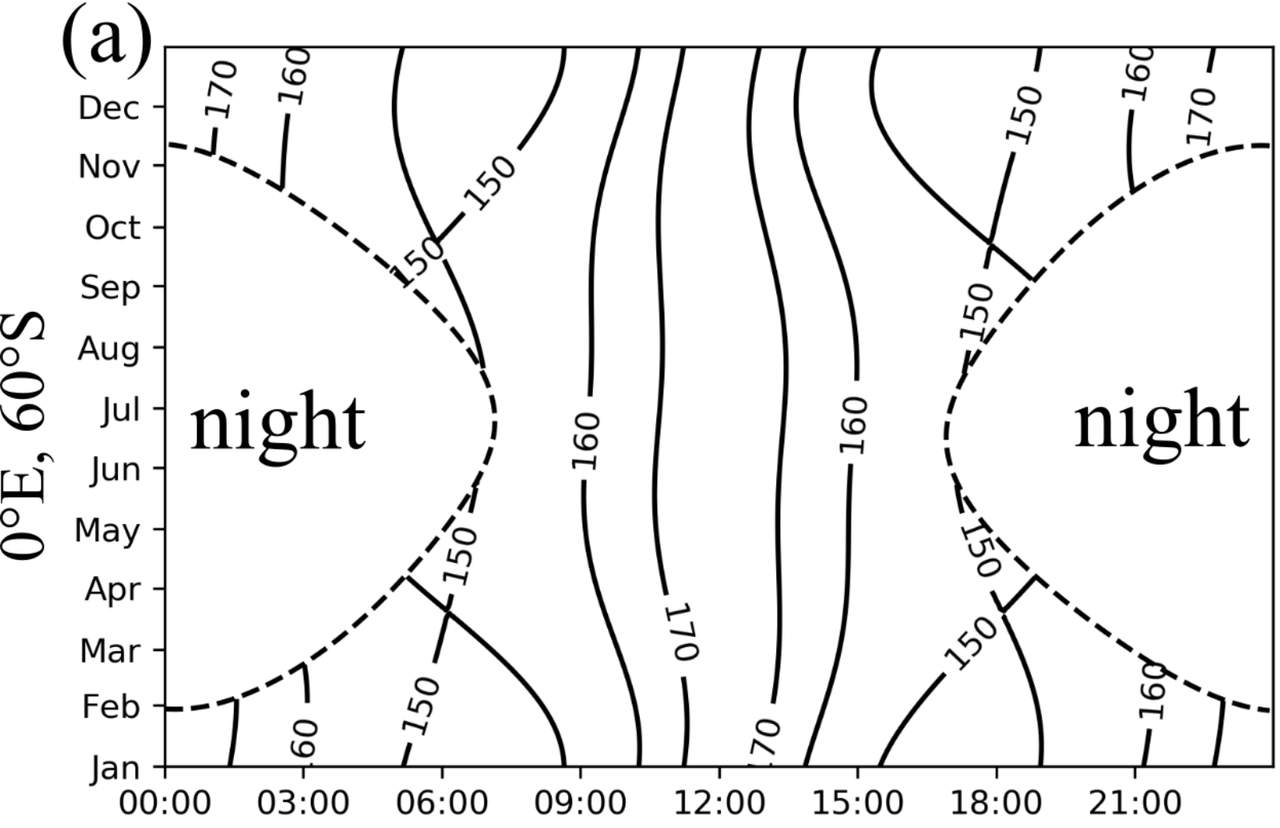
0°E, 60°S
night
night
Dec
Nov
Oct
Sep
Aug
Jul
Jun
May
Apr
Mar
Feb
Jan
00:00
03:00
06:00
09:00
12:00
15:00
18:00
21:00

(b)

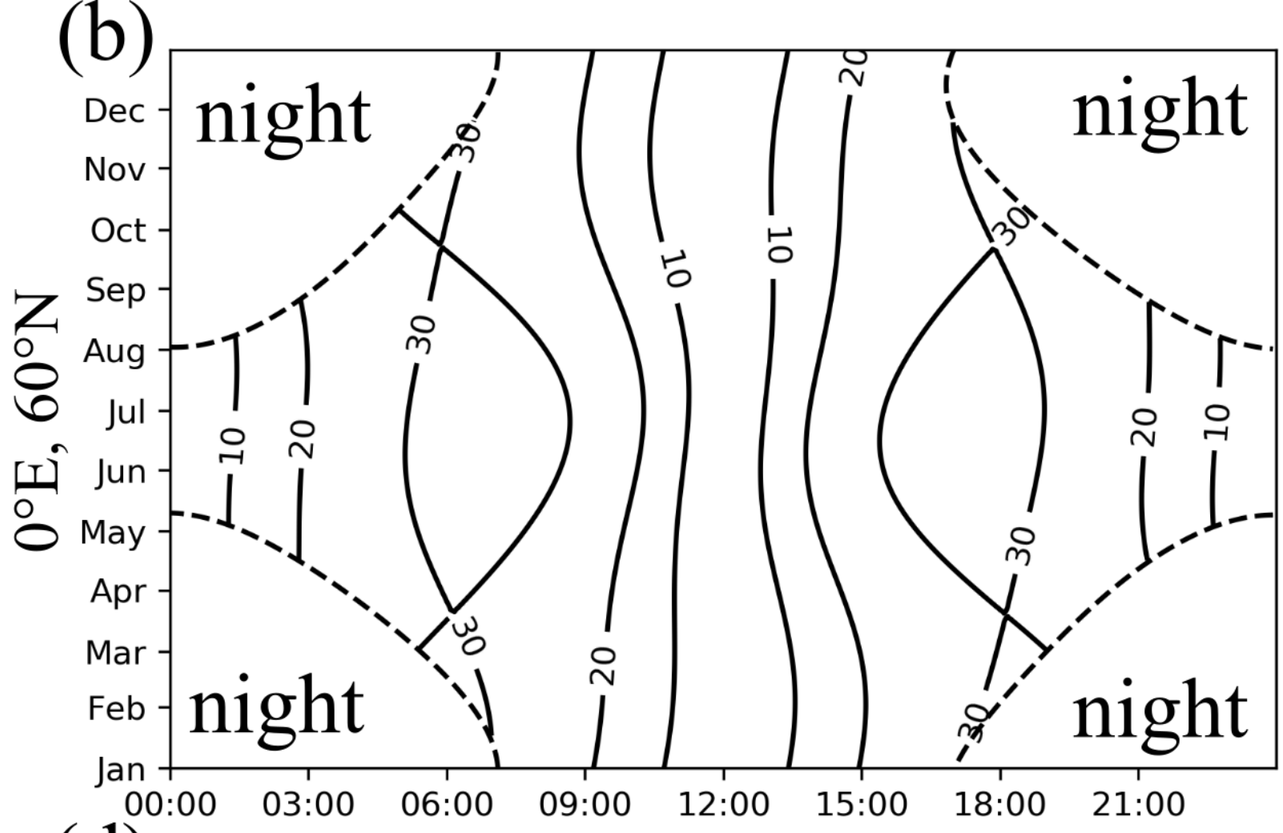
0°E, 60°N
night
night
night
night
Dec
Nov
Oct
Sep
Aug
Jul
Jun
May
Apr
Mar
Feb
Jan
00:00
03:00
06:00
09:00
12:00
15:00
18:00
21:00

(c)

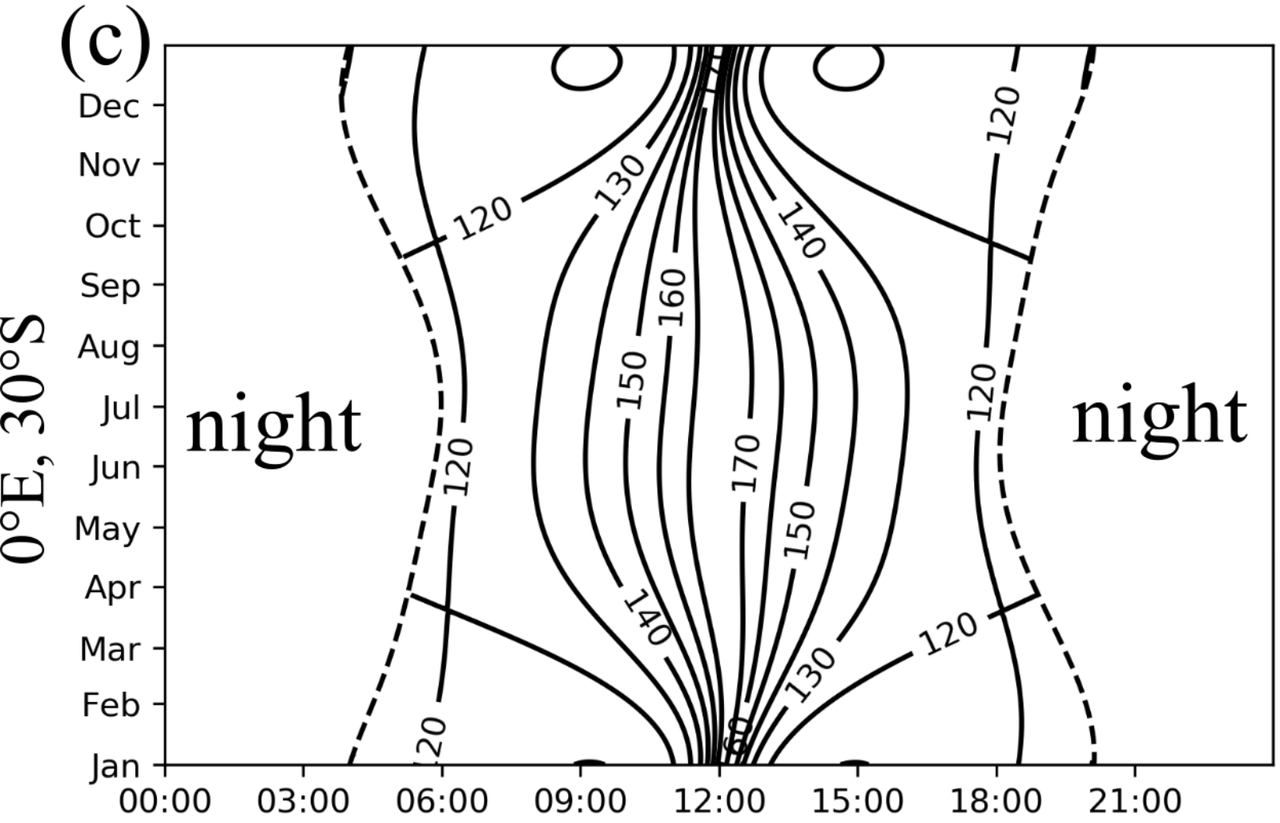
0°E, 30°S
night
night
Dec
Nov
Oct
Sep
Aug
Jul
Jun
May
Apr
Mar
Feb
Jan
00:00
03:00
06:00
09:00
12:00
15:00
18:00
21:00

(d)

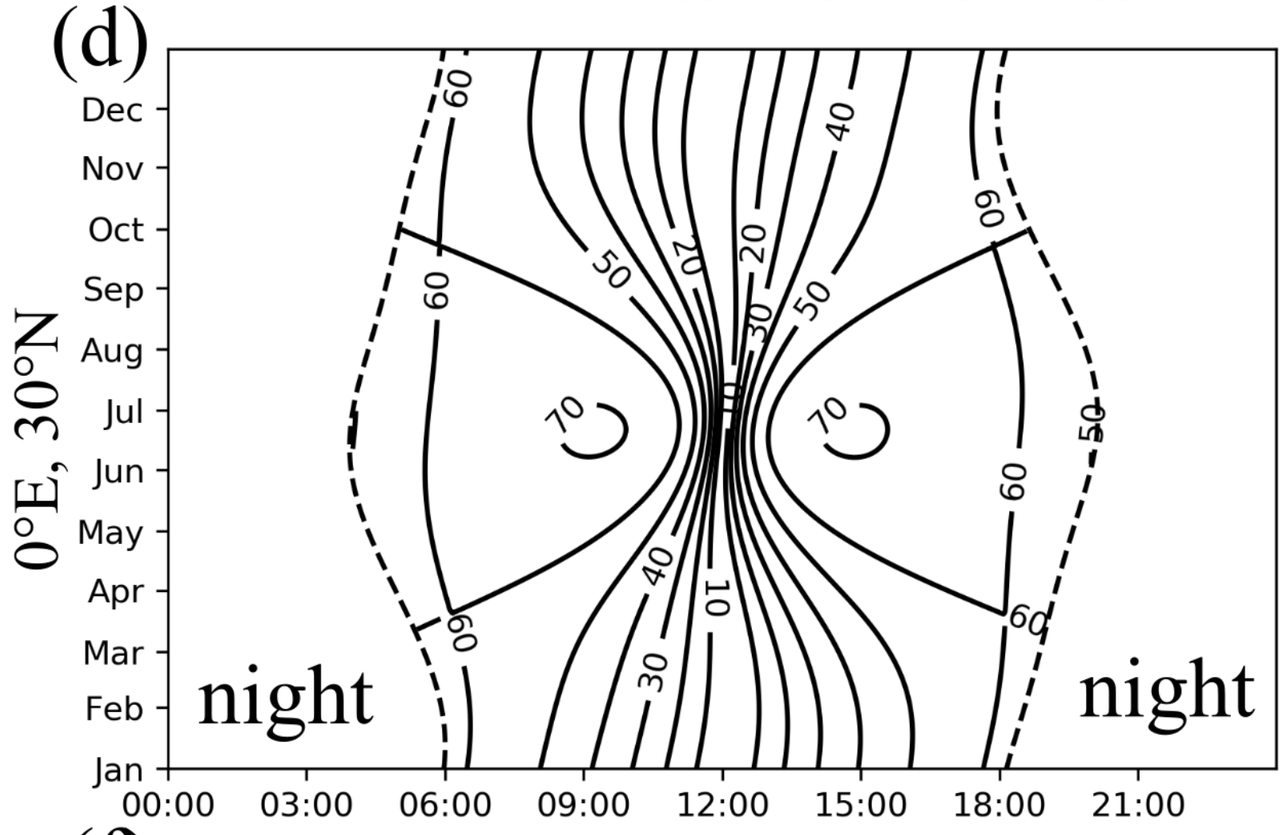
0°E, 30°N
night
night
Dec
Nov
Oct
Sep
Aug
Jul
Jun
May
Apr
Mar
Feb
Jan
00:00
03:00
06:00
09:00
12:00
15:00
18:00
21:00

(e)

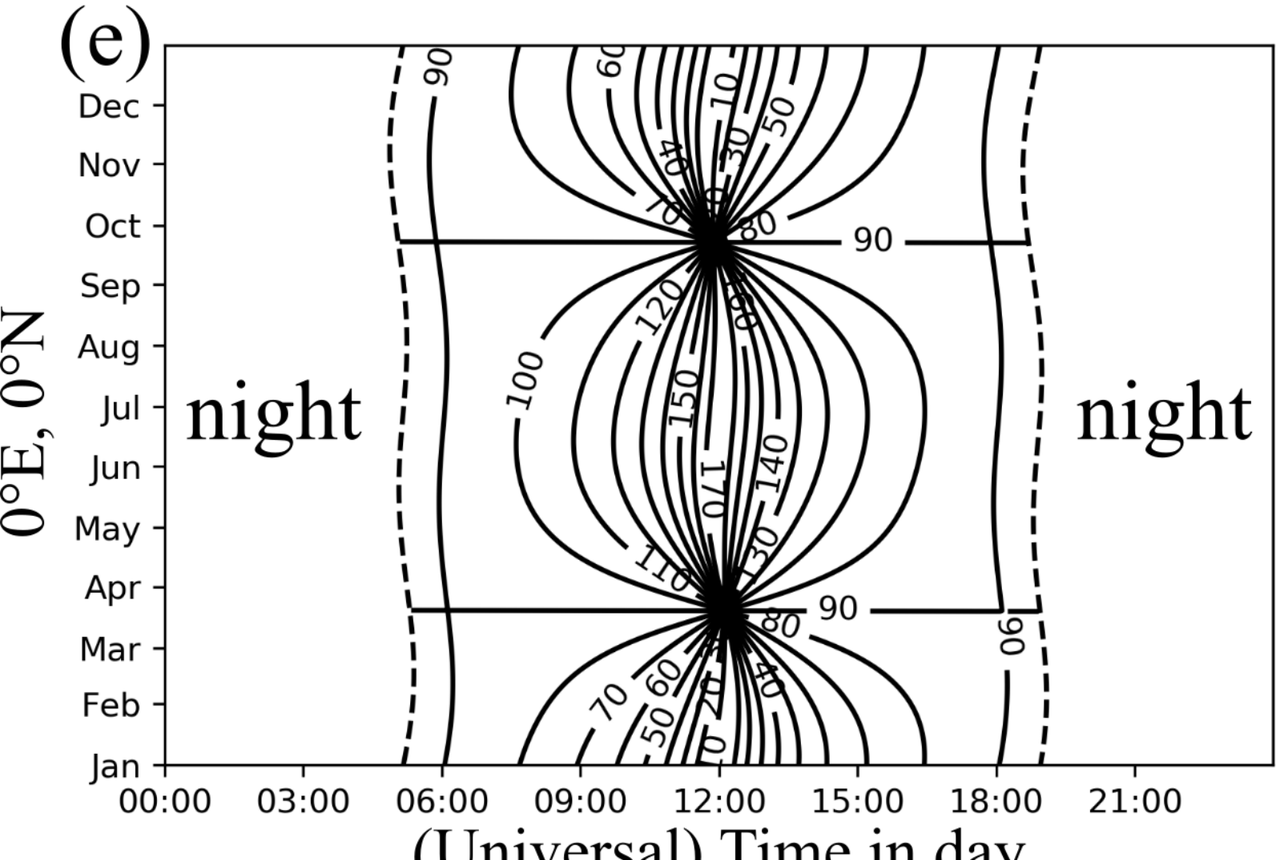
0°E, 0°N
night
night
Dec
Nov
Oct
Sep
Aug
Jul
Jun
May
Apr
Mar
Feb
Jan
00:00
03:00
06:00
09:00
12:00
15:00
18:00
21:00
(Universal) Time in day

(f)

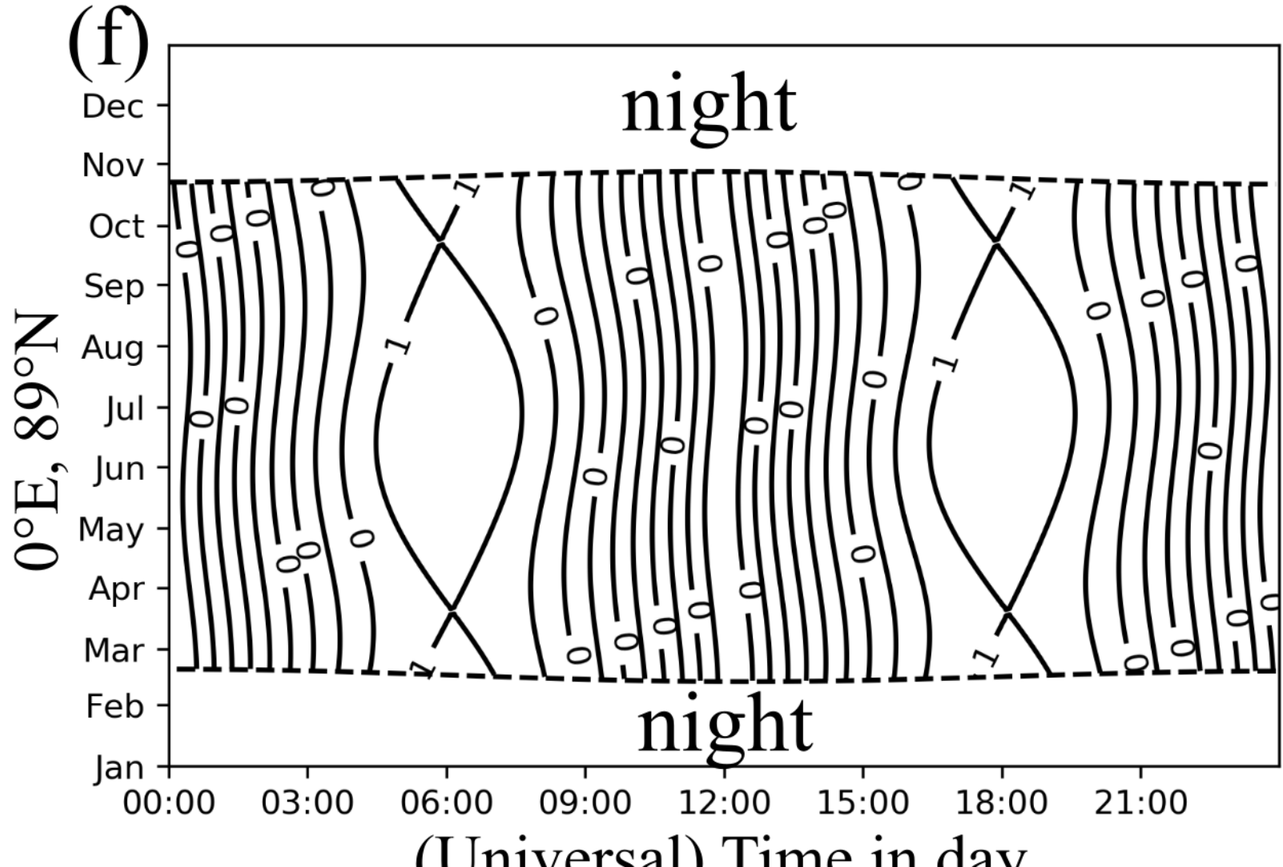
0°E, 89°N
night
night
Dec
Nov
Oct
Sep
Aug
Jul
Jun
May
Apr
Mar
Feb
Jan
00:00
03:00
06:00
09:00
12:00
15:00
18:00
21:00
(Universal) Time in day

Figure A2.

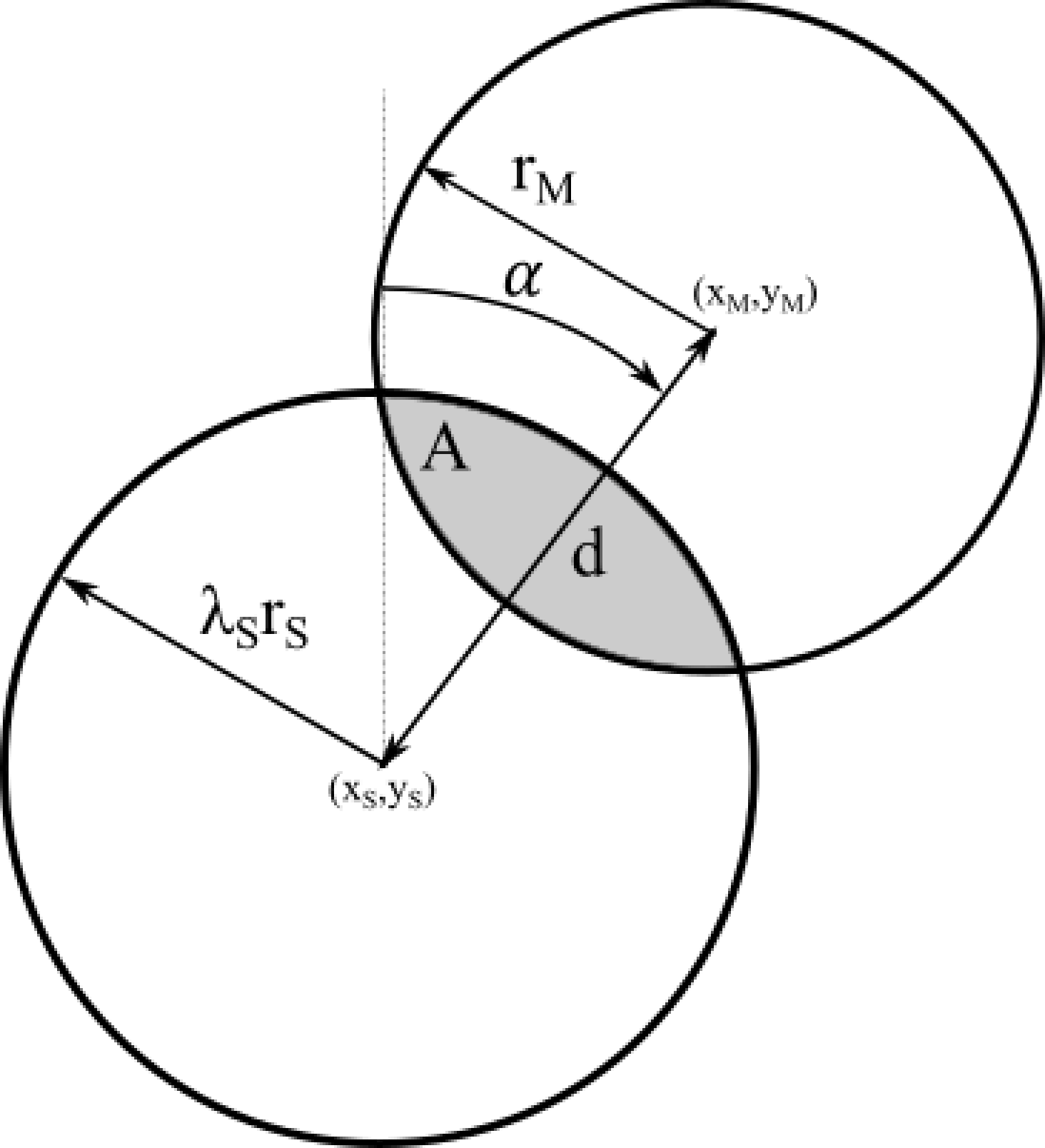
r_M
α
(x_M, y_M)
A
d
$\lambda_S r_S$
(x_S, y_S)